Characteristics of Line Focused Laser Supported Detonation

Department of Advanced Energy
Graduate School of Frontier Sciences
the University of Tokyo

Masato Ushio

February 13, 2006

Contents

List of Figures

List of Tables

Acknowledgments

I thank everyone who helped me and supported me to complete this thesis.

First I would like to appreciate my advisor, Associate Professor Kimiya Komurasaki, for his continuous and attentive guidance, support, and encouragement.

I would like to express my thanks to Professor Yoshihiro Arakwa, for giving me advice to improve my study.

I would like to express my gratitude to the members of Komurasaki Laboratory and Arakawa Laboratory for their intellectual and social contributions. Mr. Mori, Mr. Katsurayama, Mr. Hirooka, Mr. Fukuda, Mr. Oda, Mr. Kawamura, Mr. Fukui helped me while studying about the laser propulsion together. Mr. Matsui, Mr. Koizumi, Mr. Inoue, Mr. Takayanagi gave me a lot of precious advice.

Without any of these support, this thesis would not have been completed. Thank you.

Finally, I give my special thanks to my family for their financial and mental support throughout my education.

Chapter 1

Introduction

"Why do you go to the Space?"

"Why do you want to go to the Space?"

It is clear that the answers to these two questions would differ completely in these days. Even with expert knowledge in engineering, economics and international fields, people would struggle to devise an answer on the former question. On the other hand, children would shout at once to answer the latter question. This distance indicates the wall to the Space.

About a half century passing since the first human transportation, the bottleneck is still in the excessively expensive transportation system. However, many approaches have been practiced toward this wall of the gravity. I believe these endeavor will someday liberate our wish from the gravity, the wish of anybody and everybody who want to view the Earth from the Space.

This study is about one of the new innovative space transportation systems, laser propulsion.

1.1 Background

1.1.1 Laser propulsion

Laser propulsion is a candidate for a low-cost launching system, and can be considered as the mass driver, in which the vehicle is accelerated by the laser power transmitted remotely from the ground-based or space-based laser.

Laser propulsion was first proposed by Kantrovitz in 1972 soon after the invention of laser.[1] To his proposal, various studies on laser propulsion were activated especially in the U.S.A, Russia, Germany and Japan. Although Kantrovitz proposed a laser ablation rocket, in which laser beam is irradiated to an ablator on board to produce thrust, air-breathing laser propulsion has advantage over the ablation rocket type because it does not consume fuel on board, and many studies have been concentrated on this type.

From the 70's through 80's, many studies were performed for the 'flat-plate' type.[2][3][4][5] An intense laser beam was irradiated on a metallic plate surface in the atmospheric air to produce a high-pressure region on the surface as illustrated in Fig.1.1 (a).[6] Pirri *et al.* first studied a laser pulsejet with a bell nozzle illustrated in Fig.**??**(b). A laser beam was focused by a parabolic mirror to produce plasma. Expansion of the plasma drives a spherical blast wave in the surrounding air, and impulsive thrust is generated on the nozzle wall while the blast wave expands in the nozzle.

Ageev *et al.* also studied a laser pulsejet experimentally using a parabola and a conical nozzle with a 5-J-pulse CO_2 laser.[7] In DLR (German Aerospace Center), a 53-g-Bell nozzle was launched to 60 cm high using a repetitive pulse laser whose average power was 7.9 kW (the laser pulse energy was 175 J/pulse and the repetition frequency was 45 Hz).[8]

In 1998, Myrabo *et al.* published the results of their flight demonstrations using a 10-kW-class repetitive pulse CO_2 laser.[9] Their demonstrations were the world first, and recent researches on laser propulsion were activated by their report. A 'Lightcraft' used in the demonstrations is illustrated in Fig.1.1(c). An impulsive thrust is imparted on a spike nozzle, which focuses a laser beam onto a cowl to produce plasma. Its mechanisms of impulse generation are same with those in the laser pulsejet though the geometry of focusing optics is different from the Bell type nozzle. One remarkable feature of the Lightcraft design is a front intake from which the air is taken and compressed. A Laser In-Tube Accelerator (LITA)[10] is another variety of laser propulsion. LITA is a laser-driven ram accelerator where a projectile is accelerated by successive laser-induced explosions in a tube filled with a rare gas. Its thrust generation mechanisms are also quite similar to those of the laser pulsejet.

1.1.2 Our perspective of launching system by laser propulsion

Laser-powered launch system would be applicable to the material supply for the construction of a Solar Power Satellite, for example. Our scenario of a launch is introduced here to survey the overall picture of the system.

Payload is launched through three modes; "pulsejet mode", "ramjet mode", and "rocket mode", as shown in Fig.1.2. In initial stage of a launch, the vehicle closes the inlet and takes the air from the rear side. This mode is "pulsejet mode". When the ram-compression of the inlet air becomes available as the vehicle velocity increases, the inlet is opened and the flight mode is switched to "ramjet mode". When the vehicle cannot breathe sufficient air at high altitudes, the flight mode is switched to "rocket mode" and the working fluid is changed to the hydrogen on board. Impulsive thrust is generated by the laser-induced explosion in all the propulsion modes.

A vertical launch is one of the ways to minimize the development cost of the laser base. And vertical launch to GEO by the trajectory shown in Fig.1.3 was proposed in previous study.[11][12] In this trajectory, the vehicle is accelerated to reach the orbit beyond GEO. At the apogee point, the vehicle is kicked to GTO by an on-board motor and decelerated at the perigee point as well. If the vehicle is boosted to have the velocity of 10.85km/s, the necessary velocity increment by its on-board motor is only 2km/s, which will be achieved by electric propulsion. Figure 1.4 shows the vehicle acceleration history calculated by an engine cycle analysis. The vehicle is gradually accelerated from the sea-level up to 350 km above sea level, and it will not suffer from excessive aerodynamic heating and load. As a result, 10 to 50% of the payload ratio (depending on the laser power) was estimated to be achievable.[13]

1.1.3 Thrust generation process in laser propulsion

The over-all impulse generation processes for laser propulsion are divided into four processes as shown in Fig.1.5.

1. Laser heating of the working gas
2. Blast wave energy conversion
3. Blast wave expansion in the nozzle (impulse generation)
4. Refill of the working gas

Laser breakdown of the atmospheric air is initiated by focusing an intense laser pulse. The power density threshold for the breakdown was measured at the order of 10^3 to 10^4 MW/cm^2 using a CO_2 laser. Laser breakdown process and laser-induced plasma generation process are as follows.[14] In the first stage, N_2 and O_2 molecules in the air are ionized by multiphoton absorption. This phenomena occurs when the simultaneous absorption energy of n photons, $nh\nu$, exceeds the ionization potential, where h stands for the Planck constant and ν stands for the frequency of the light. The minimum ionization

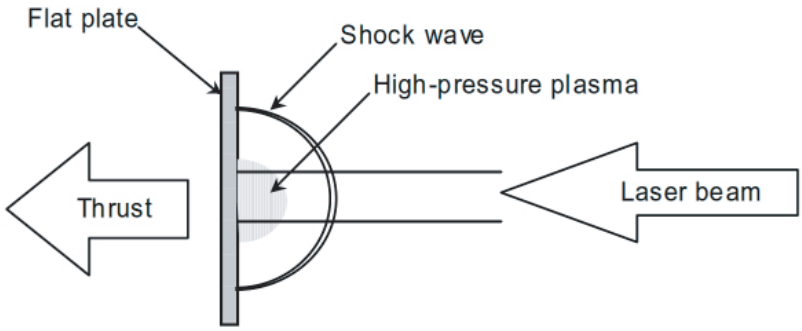

(a) Flat plate type laser propulsion

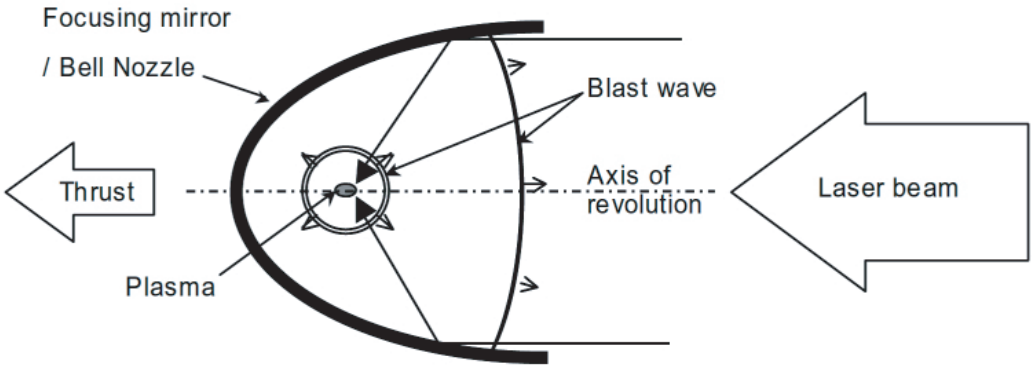

(b) Laser pulsejet with a Bell nozzle

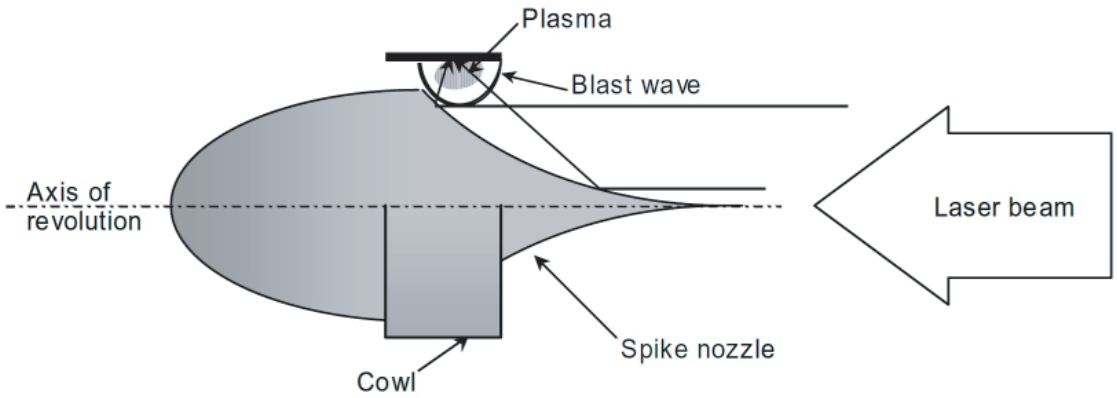

(c) Lightcraft designed by Myrabo

Figure 1.1: Schematic of different varieties of laser propulsion.

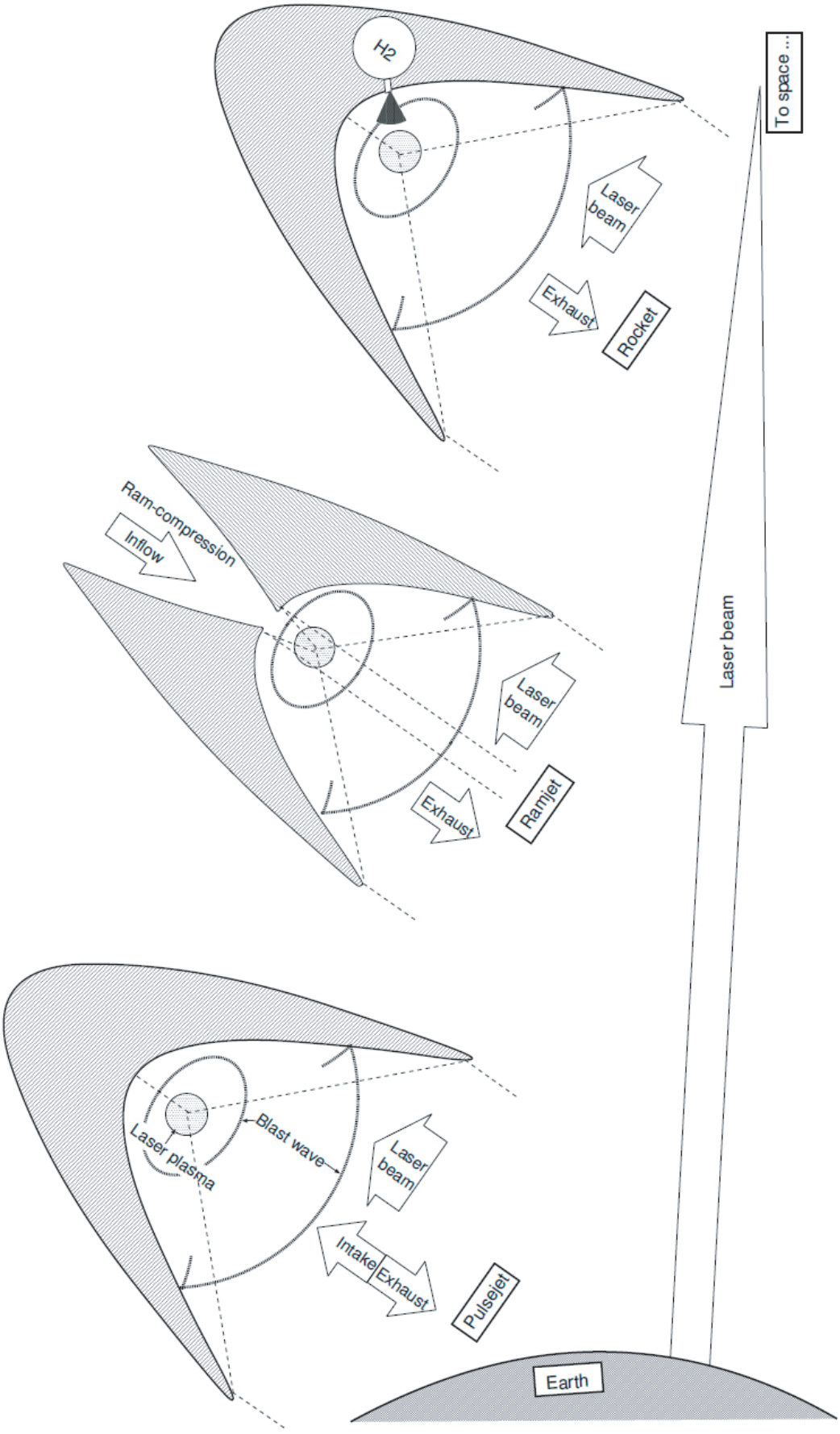

Figure 1.2: 3 modes of laser-powered lanch system.

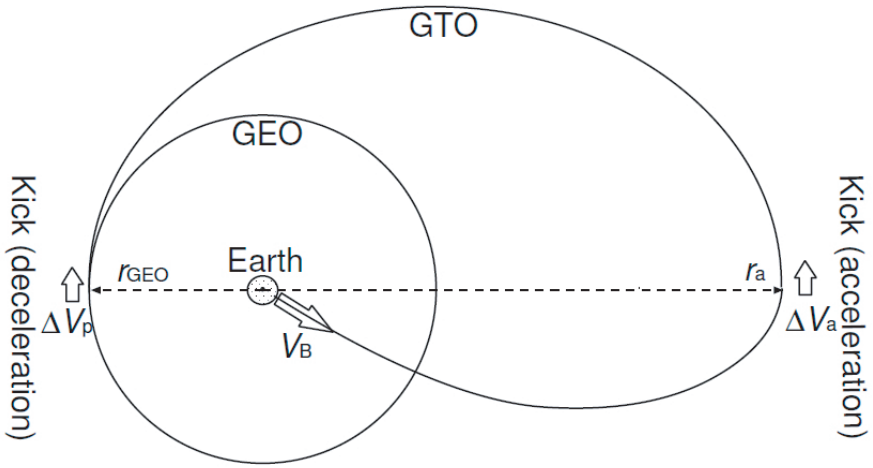

Figure 1.3: Trajectory to GEO.

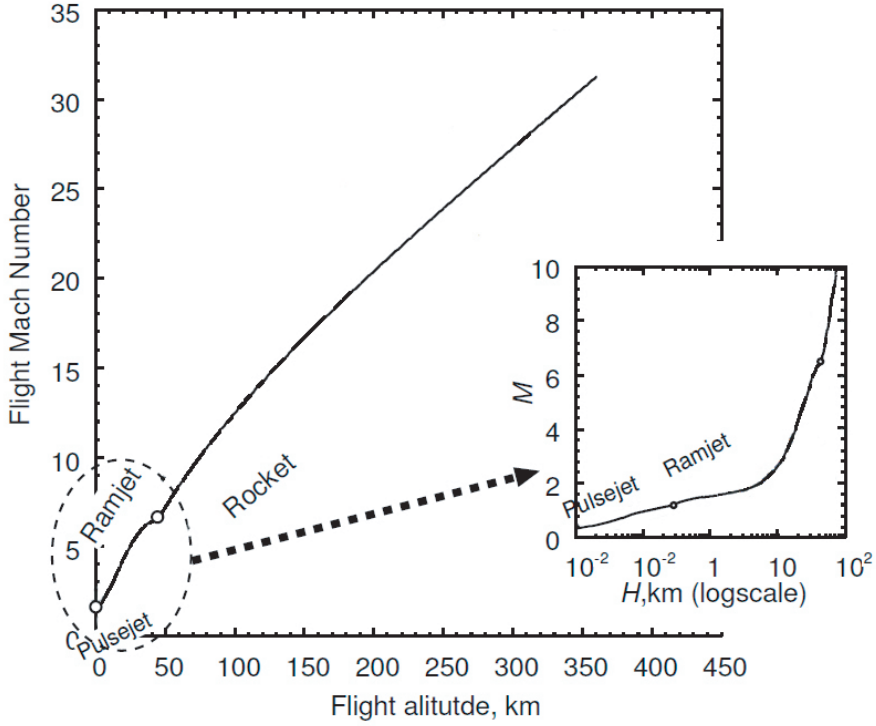

Figure 1.4: The vehicle acceleration history for the vertical launch to GEO.

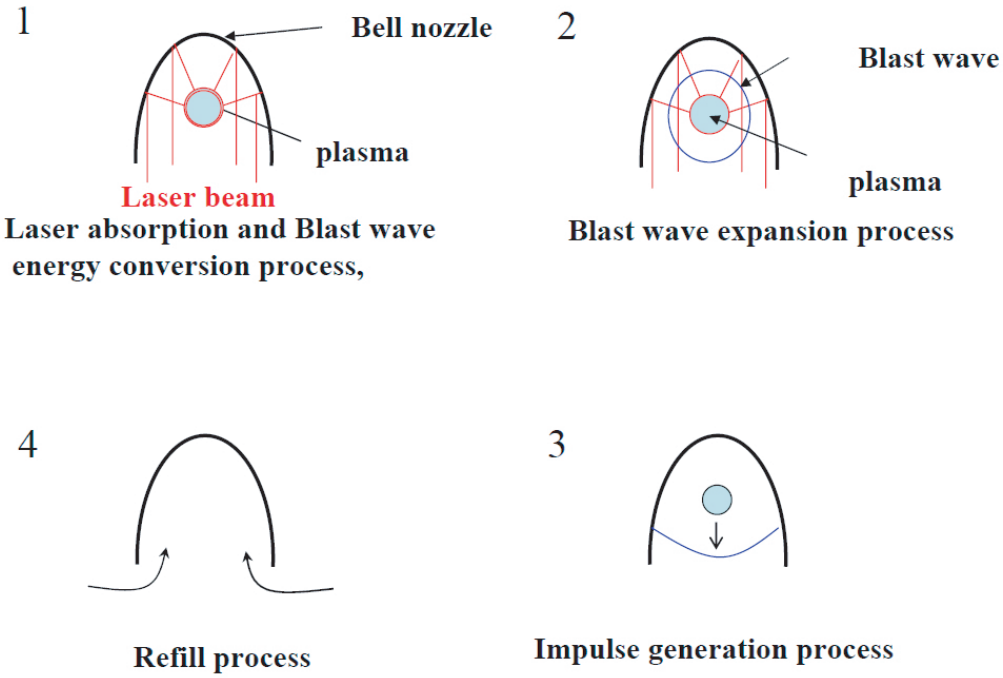

Figure 1.5: Engine cycle of laser pulsejet.

energies of O_2 and N_2 are 12.5eV and 15.8eV, so it could be estimated as n=11 for O_2 and n=14 for N_2 for a CO_2 laser. The electrons generated in this first stage are called the first generation electrons. In the second stage, the first generation electrons, being accelerated by the inverse-bremsstrahlung effect, remove electrons from the other molecules and atoms. In this way, an electron avalanche develops. When the characteristic length of the ionization regime is parallel to the Debye length, a laser-induced plasma generates. When the intense laser beam continues to irradiate on the surface of this plasma, the laser energy is absorbed mainly through the inverse bremsstrahlung process. It is well known that the laser absorption mechanism is classified into two regimes. At the laser power densities greater than the order of 10 MW/cm^2, the laser absorption occurs in Laser Supported Detonation (LSD) regime.[15][16][17] On the other hand, at the power densities lower than 1 MW/cm^2, it occurs in Laser Supported Combustion (LSC) regime.

In LSD regime, a laser absorbing region propagates at a supersonic velocity inducing a strong blast wave, along the laser light channel in the direction opposite to the beam incidence. This phenomenon is called LSD wave. Although the mechanism of LSD wave propagation is not clarified, the existence of "priming" electrons in the front of the strong laser absorption regime is considered to be important. The priming electron is considered to be produced by mainly three effects as follows.

1. Shock compression effect.

   Similar to chemical detonation wave, LSD wave is thought to have a Zel'dovich-Nuemann-Doring (ZND) wave structure, in which cold gas ahead of the wave is compressed and heated in a shock front called the von-Neumann spike.[18]

2. Photoionization or photoexcitation effect.

   In general, very high temperature region radiate the ultraviolet-ray. The high energetic photon emitted from this region could directly remove or excite electrons of the molecules in the cold gas ahead of the thermal boundary layer. This is called photoionization and photoexcitation.

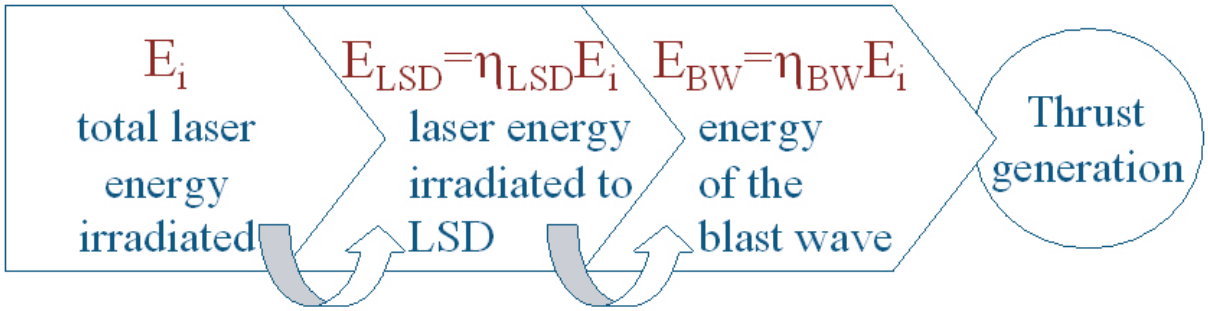

Figure 1.6: An energy flow from laser to blast wave.

3. Electron diffusion effect.

   By the diffusion of the electrons with very high energy, the laser absorption precursor is generated ahead of LSD front. This effect is reported to be essential to generate LSD wave in room temperature by Shiraishi.[19]

The dominant effect in the three effects varies depending on the laser power density irradiated on the LSD front.

In the LSC regime, laser absorption region propagates in the direction opposite to beam incidence at a subsonic velocity due to heat conduction. The absorption wave has a structure similar to a deflagration wave, and it is called an LSC wave. The laser energy absorbed in LSC wave has no contribution to the blast wave induction. The laser energy absorbed in this regime may be converted into the radiation energy and the internal energy frozen in the plasma region remained in the center of the blast wave expansion.

To determine a single-pulse thrust performance of air-breathing pulse laser propulsions, momentum-coupling coefficient C_{m} defined as Eq.(1.1) is convenient,

$$C_{\mathrm{m}} \equiv \frac{I}{E_{\mathrm{i}}} \tag{1.1}$$

where I is the impulse and E_{i} is the irradiated laser pulse energy.

There are two important parameter that dominate the C_{m} as seen here; η_{LSD} and η_{BW} which are expressed as,

$$\eta_{\mathrm{LSD}} = \frac{E_{\mathrm{LSD}}}{E_{\mathrm{i}}} \tag{1.2}$$

$$\eta_{\mathrm{BW}} = \frac{E_{\mathrm{BW}}}{E_{\mathrm{i}}} \tag{1.3}$$

where E_{i} is total laser energy irradiated, E_{LSD} is laser energy irradiated to LSD, and E_{BW} is energy of the blast wave which is defined as the source energy necessary to drive an equivalent blast wave in a calorically perfect gas, as in the ideal case of blast wave expansion. This concept is mentioned in detail in the following chapter. Using these efficiencies, the rate of the blast wave energy to the energy absorbed in the LSD region is expressed as $\eta_{\mathrm{BW}}/\eta_{\mathrm{LSD}}$.

Figure 1.6 shows an energy flow from the laser to the blast wave. As seen in the figure, the laser energy is converted to the energy of the blast wave at first, and then to the thrust. And the conversion from the laser energy to the blast wave energy occurs mainly in the laser supported detonation, LSD. It is clear that the higher E_{LSD} (higher energy absorption in the LSD regime) leads to the higher E_{BW}(higher energy conversion to the blast wave), and the higher E_{BW} leads to the higher C_{m}.

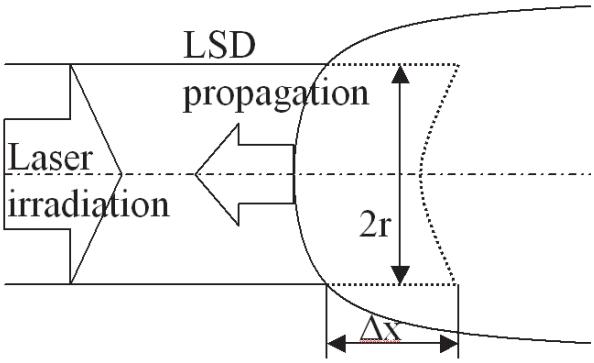

Figure 1.7: Schematic of a lateral expansion of an LSD.

1.1.4 Theory of LSD termination

As seen in the previous section, sustention of the LSD is effective in increasing the thrust performance of laser propulsion. The theory of LSD termination by Raizer[20] is introduced in this section.

As seen in the Fig.1.7, heated and compressed gas in the zone where the LSD takes place expands not only along the direction of propagation of the shock wave, which causes the motion of this wave, but also in the lateral directions. This lateral expansion uses some of the energy which will not help the propagation of the detonation wave. The ratio of the energy lost as a result of this lateral expansion to the energy utilized in the propagation of the detonation is characterized by the ratio of the lateral surface $2\pi r\Delta s$ to the area of the wave front πr^2, i.e., it is characterized by the ratio $\Delta x/r$. Δx is the order of the path traveled by the incident radiation l. If the thickness l is of the order of or greater than r, the energy losses by the lateral expansion are so large that the input laser energy is insufficient to sustain the initiation shock wave. In practice, Raizer predicted that an LSD would terminate when $l/r \approx 4$.

In Raizer's theory, laser light channel geometry is one dimensional. However, in the laser propulsion, LSD is mainly generated in the cone shaped laser channel. In order to represent the ratio of energy lost by the lateral expansion to the energy utilized, a ratio

$$S_{\text{side}}/S_{\text{front}} \tag{1.4}$$

would be accurate in the case the geometry of the laser light channel differs. In this expression, Raizer's prediction of LSD termination would be as follows: LSD would terminate when $S_{\text{side}}/S_{\text{front}} \approx 8$. In this theory, LSD termination is determined only by the energy loss due to lateral expansion. This indicates the possibility of preventing the LSD termination by confining the lateral expansion.

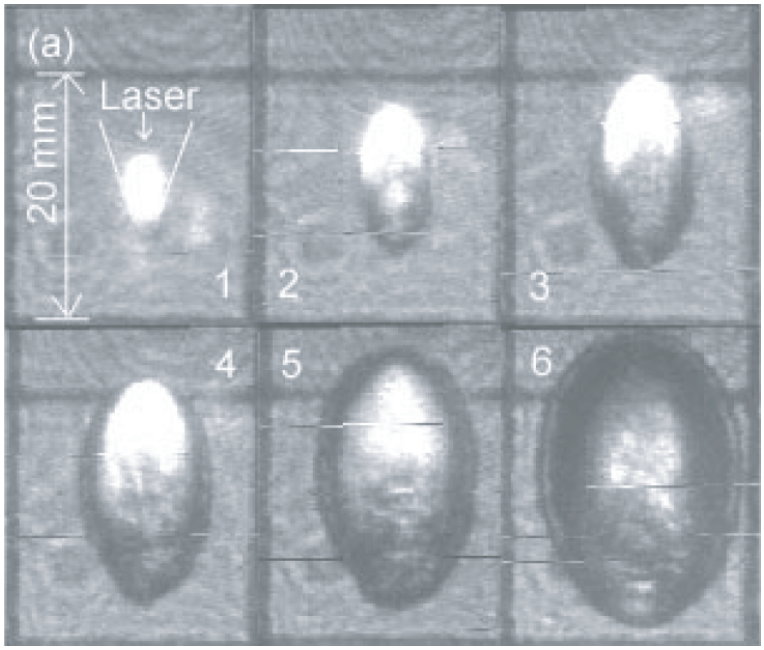

Figure 1.8: The shadowgraphs of the LSD wave driven by a point-focused laser.

1.2 Scope of this study

High C_{m} in the three launching modes will assure the system feasibility and reduce the infrastructure cost. The energy conversion efficiency must be characterized in order to define the room of the C_{m} improvement. The conversion efficiency from blast wave energy to C_{m} could be calculated and be optimized numerically, by applying the established CFD technique. However the energy conversion characteristics from laser to blast wave are not well known. As LSD is one of the key phenomenon in this energy conversion process, the knowledge of the fundamental physics of LSD and it's sustention, such as the characteristics of η_{BW} and η_{LSD}, is necessary for predicting C_{m} in various conditions.

To introduce the scope of this study, some of our previous studies which were related to the LSD are shown below.

1.2.1 Our previous studies

Mori *et al.* [21][22] characterized the blast wave driven by a point-focused laser beam by shadowgraph method (Figs.1.8 and 1.9). They evaluated the laser intensity threshold S_{LSD} at LSD termination and the blast wave energy E_{BW} by the analysis of temporal variation of the shock wave front, ionization (plasma) front.

They also measured the energy loss by plasma radiation, as seen in the Fig.1.10. While the blast wave energy conversion efficiency was 47%, over 20% of the energy irradiated on the LSD front was lost as radiation loss. The left 30% of the energy was assumed to be the chemical frozen loss due to the high temperature area remained behind. One of the reasons for these losses may be the result of excessively high temperature at the LSD plasma due to the excessively high laser intensity at the LSD front. There is a possibility of reducing them by decreasing the peak laser intensity at the LSD front.

Considerable relation between ambient pressure and η_{BW} was observed as seen in Fig.1.11. The relation similar to this is seen also in many other studies[23],[24]. This indicates that η_{BW} could be increased by controlling the pressure. One of the ways to control the pressure is to confine the blast wave into the narrow area by using a boundary such as a cone nozzle, in order to prevent the fast pressure

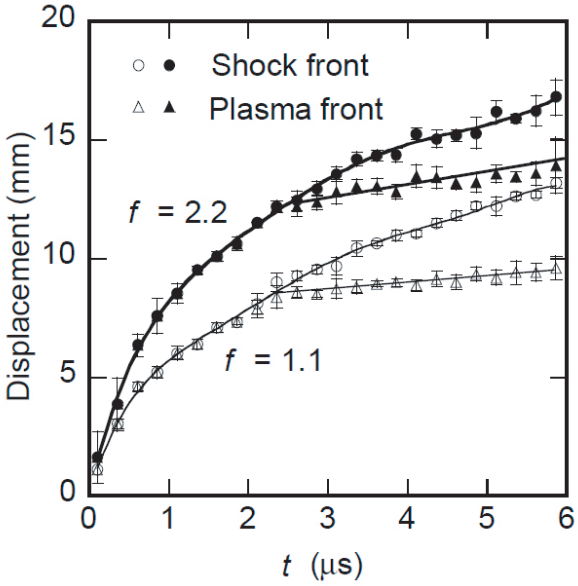

Figure 1.9: The temporal variation of the shock front and the plasma front.

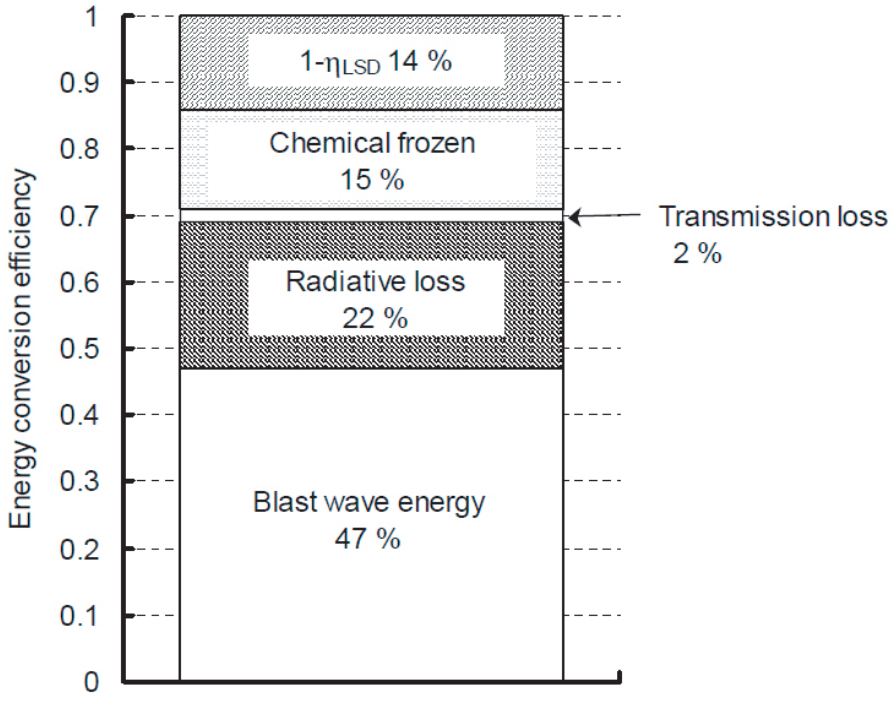

Figure 1.10: The energy conversion efficiency of a point-focused laser LSD.

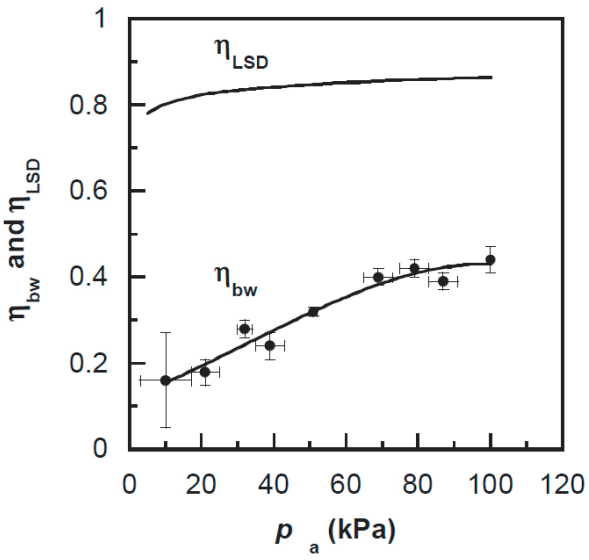

Figure 1.11: The relation between ambient pressure and η_{BW}.

decrease as a result of the wide expansion of the LSD induced blast wave. However, the blast wave in the cone nozzle cannot be simply visualized (or characterized). This means that the LSD termination laser intensity threshold or blast wave energy cannot be measured by the same method to this study. Therefore some improvement is necessary to consider the effect of a blast wave confinement to the LSD sustention.

Mori's study clarified the dependence property of LSD to some property of the surrounding condition, by the measurement of energy conversion efficiency. On the other hand, Fukuda *et al.* [25] investigated the electron density distribution in the LSC regime using the Mach-Zehnder interferometry(Fig.1.12), in order to clarify the relation between the energy conversion efficiency and the electron density of LSD. (Since CO_2 laser beam is absorbed mostly by the electrons through the inverse-bremsstrahlung process, the fractional absorption of laser power correlates closely with electron density in the absorption layer, whose length is critical for LSD sustention.) These relation could be used to construct the appropriate physical model, which would be useful for the performance prediction of high power laser propulsion in unusual circumstances, such as in ramjet mode or rocket mode. Peak electron number density of $10 \times 10^{24}/m^3$ order was observed in the LSD regime in this experiment. However, the interferograms of the LSD region was unable to analyze, because of strong refractive effect in the LSD as seen in Fig.1.13. Therefore another improvement is necessary to observe the electron density distribution in the LSD regime.

In these experiments, the blast waves were driven by a point focused laser beam. However, to realize really high power laser vehicles, a line-focusing technique would be inevitable. In line-focusing optics, laser intensity at the focal line is controllable, and there is a possibility of reduction in radiation and frozen flow losses because the peak intensity in the vicinity of focal line can be lowered compared with the point focused case. The line-focusing technique has also been used in a Lightcraft which was mentioned above.[9]

1.2.2 Line focused LSD

Considering these facts, line focused LSD was investigated in this study. In this section, this is explained in detail.

In line focused LSD, a LSD is generated by the laser focused on the line as seen in Fig.1.14(the laser

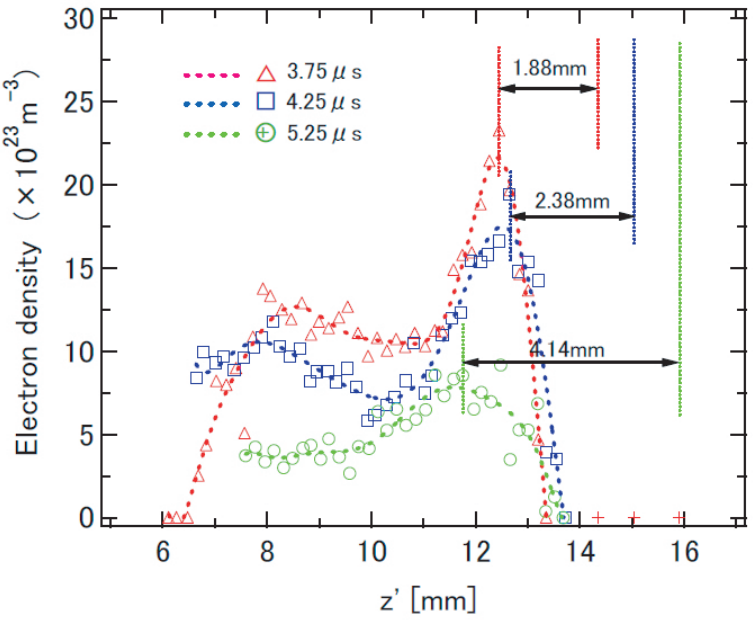

Figure 1.12: The interferograms of the LSC.

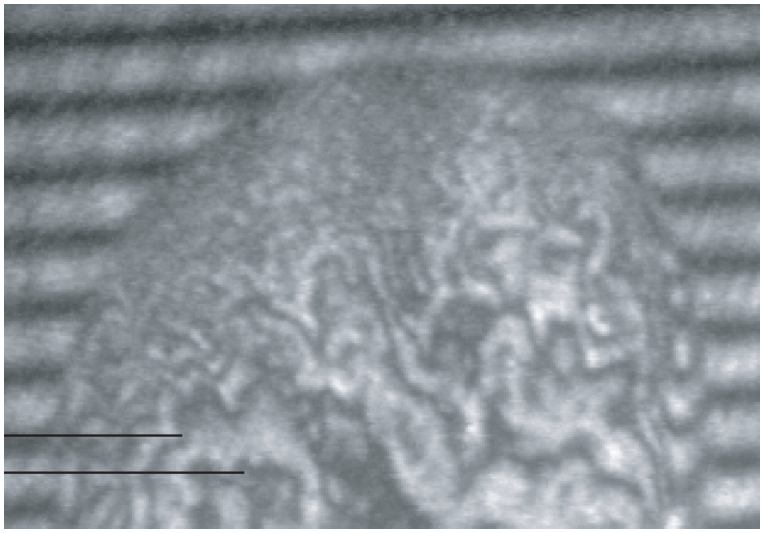

Figure 1.13: The interferogram of the LSD region.

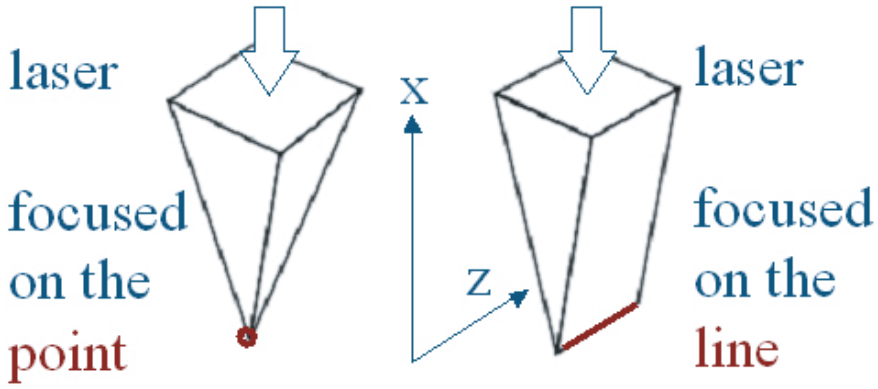

Figure 1.14: The concept of line and point focused laser.

focused on the point is shown for comparison). It is clear that the line focused laser

- has lower intensity at the focus.
- has moderate gradient of irradiation area while the LSD propagation.
- is uniform in z direction (as in the figure).

These characteristics are useful for the following reason.

1. It has a possibility of reducing the energy conversion losses by decreasing the peak laser intensity at the LSD front, while sustaining the LSD by moderate gradient of the intensity.
2. One direction could be used to confine the LSD, while uniform z direction could be used for visualization. Thus, effect of a blast wave confinement to the LSD sustention could be characterized by measuring the conversion efficiency of the line focused LSD confined by two dimensional wedge nozzle.
3. In various kinds of optical visualization methods, a probe light is affected while passing through the phenomena. In these cases, the quantitative factors as typified by the thickness of phenomena, as well as the qualitative factors (such as density, temperature, etc.) are dominating the visibility of the phenomena. Strong refractive effect, as in the Fukuda's case, could be modified by changing the width of the phenomena. And in line focused LSD, the width of the phenomena could be changed easily because of the uniformity in z direction.
4. Smaller dimension has an advantage in simple numerical analysis as well as for the analysis of the experimental results.

In addition, line focused LSD is important to realize RP laser propulsion by high power laser as mentioned before.

1.3 Objectives

In this study, line focused LSD was measured by shadowgraph method and Mach Zehnder interferometry. Objectives of this study is to

1. characterize the fundamental characteristics of line focused LSD,
2. measure the effect of LSD confinement,
3. visualize the interferogram of the blast wave in LSD region,
4. relate the LSD termination and density distribution of electron and neutral, in LSD region.

Chapter 2

Mach Zehnder interferometry

Two-wave Mach Zednder interferometry was applied in this study. Principle of Mach Zehnder interferometry, it's application as two-wave Mach Zehnder, and the way to analyze the interferogram is shown in this chapter.

2.1 Principle of Mach Zehnder Interferometry

Mach Zehnder interferometry is one of the quantitative visualization methods. In Mach Zehnder interferometry, coherency of light is used to determine the refractive index. Thus it has following characteristics.

1. It is noncontact method for measurement.
2. It responds fast enough to acquire the nonsteady phenomena.
3. It is applied only for a gas or a liquid which is transparent to the probe light.
4. It cannot detect the little density area with little refractive index.

The system of the Mach-Zehnder interferometry consists of two beam splitters and two plane mirrors as shown in Fig.2.1. A homochromatic light from the light source is divided into two, and recombined on a screen. With slight difference in light path lengths, two lights interfere each other and make a interferometric fringe pattern. Where the difference in light path length is the same to $\lambda \times n$ (λ is wavelength, n stands for positive integer), they reinforce each other and become bright because two lights are in phase. On the other hand, where the difference is the same to $\lambda \times (n + 1/2)$, they cancel each other and become dark. When one of the lights propagates through the target object, difference of the refraction index in the object will be visualized quantitatively in the form of fringe pattern shift. (Thus one of the two lights is called a reference light and the other is called a probe light.) This fringe pattern shift is expressed as

$$h = \frac{1}{\lambda} \int \left(N_{\mathrm{ref}}(z) - N_{\mathrm{flow}}(z) \right) dz \tag{2.1}$$

where h is the number of fringe shift, z is the direction of the channel of the probe laser beam, N is the refractive index, λ is the wavelength of the light source. The subscripts "flow " and "ref" represent the case inside and outside(reference path) of the test section respectively. When the flow in the test section was homogeneous, with width of d, Eq.(2.1) could be rewritten as

$$h = \frac{\left(N_{\mathrm{ref}}(z) - N_{\mathrm{flow}}(z) \right) d}{\lambda} = \frac{\Delta N d}{\lambda} \tag{2.2}$$

$$\Delta N = \frac{h\lambda}{d} \tag{2.3}$$

where ΔN is the difference of the refractive index between the reference area and the object. Thus just by reading the shift of a fringe pattern, refractive index inside the target object will be known.

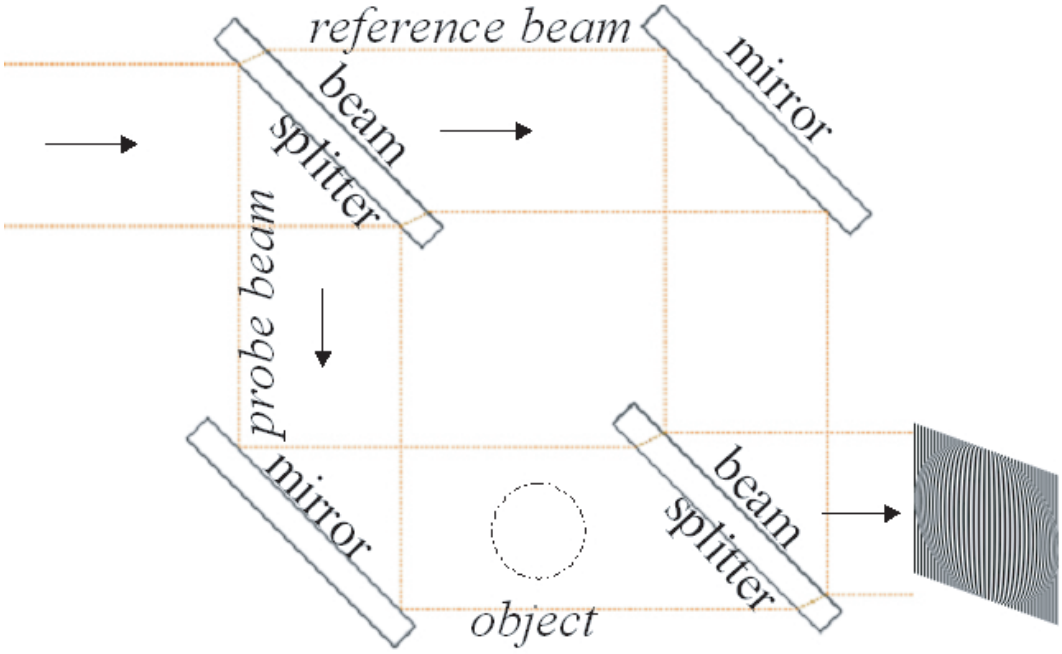

Figure 2.1: The fundamental system of Mach Zehnder interferometry.

2.2 Refractive index

A refractive index is defined as the ratio of the phase speed of the light in a given medium and in a vacuum. In this study, this medium corresponds to laser-induced plasma which consists of electrons, ions and neutral particles, and a blast wave which consists of neutral particles. In general, the refractive index N of the medium consisted of many species is approximately expressed as follows

$$N - 1 = \sum K_j n_j \tag{2.4}$$

where K_j and n_j are the relative refractive index and the number density of species j respectively. The medium in this study are consisted of three species; an electron, an ion, a neutral particle. The relative refractive indices of an ion and a neutral particle is approximately constant; K_i=7.4×10^{-30} [m^3], K_n=1.1×10^{-29}[m^3]. On the other hand, the relative refractive index of electron is dependent on the wave length as seen in the Fig.2.2.[26] And its value is estimated from the dispersion relation of the electromagnetic wave propagating in plasma under the assumption of no magnetic field. The dispersion relation is as follows,

$$\omega^2 = \omega_{pe}^2 + k^2 c^2 \tag{2.5}$$

$$\omega_{pe} = \sqrt{\frac{n_e e^2}{m_e \varepsilon_0}} \tag{2.6}$$

where ω, k is the angular frequency and the wave number of the electromagnetic wave in a plasma, respectively, and ω_{pe} is the plasma frequency. c, ε are the light velocity and the permittivity of free space, and n_e, m_e, e are the electron number density of the plasma, the electron mass and electron charge, respectively. The refractive index of an electron to the electromagnetic wave of angular frequency ω, is

$$N_e = kc/\omega \tag{2.7}$$

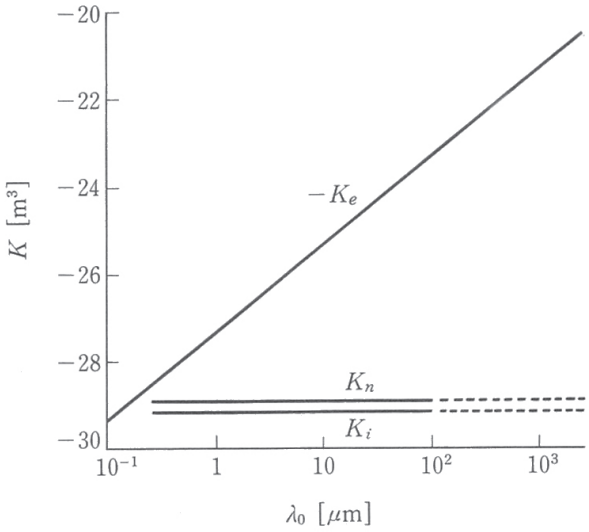

Figure 2.2: The dependence of the refractive indices on the wave length.

Using Eqs.(2.5) and 2.7, the following equation are derived.

$$N_e = \left(1 - \left(\frac{\omega_{pe}}{\omega}\right)^2\right)^{1/2} \tag{2.8}$$

Under the additional assumption, Eq.(2.5) is

$$N_e - 1 = -\frac{\omega_{pe}}{2\omega^2} \tag{2.9}$$

From Eq.(2.4), the relative refractive index is expressed as follows

$$K_e = -\frac{e^2}{8\pi^2 c^2 m_e \varepsilon_0}\lambda^2 \tag{2.10}$$

where λ is the wavelength of the electromagnetic wave. As seen in Eq.(2.10), -K_e is proportional to the square of the wavelength. By Eqs.(2.3) and (2.4),

$$\Delta N = \frac{h\lambda}{d} = \sum_{\text{ref}} K_j n_j - \sum_{\text{flow}} K_j n_j \tag{2.11}$$

$$= K_n n_0 - K_n n_n - K_i n_i - K_e n_e \tag{2.12}$$

where K is a relative refractive index and n is a number density. Subscripts, n, i, e, represent neutral particles, ions and electrons respectively. n_0 is the number density of the neutral particle in the atmospheric air (reference path was set in the atmospheric air).

Without any assumption, contribution of the number density of each particle to the total refractive index cannot be identified from simple Mach Zehnder interferometry and this equation. However, by using the dependency of K_e to the wavelength, contribution of the electron density would be extracted. This is described in the next section in detail.

2.3 Two-wavelength Mach Zehnder interferometry

The large dependence of the electron component and the relatively small dependence of the other plasma constituents on the probe light wavelength make it possible to determine electron density, even in the

presence of contributions to the refractivity from the nonelectronic constituents. This is accomplished by simultaneous measurement of the refractive index of the plasma at two wavelength.[27] By two-wavelength Mach Zehnder interferometry using the wavelength λ_1 and λ_2, ΔN_1 and ΔN_2 would be known from Eq.(2.12) and 2.10 as follows,

$$\begin{aligned} \Delta N_1 &= K_n n_0 - K_n n_n - K_i n_i - K_{e1} n_e && (2.13) \\ &= K_n n_0 - K_n n_n - K_i n_i - \left(-\frac{e^2}{8\pi^2 c^2 m_e \varepsilon_0} \lambda_1^2 \right) n_e && (2.14) \end{aligned}$$

$$\begin{aligned} \Delta N_2 &= K_n n_0 - K_n n_n - K_i n_i - K_{e2} n_e && (2.15) \\ &= K_n n_0 - K_n n_n - K_i n_i - \left(-\frac{e^2}{8\pi^2 c^2 m_e \varepsilon_0} \lambda_2^2 \right) n_e && (2.16) \end{aligned}$$

where K_1 and K_2 is the relative refractive index of the electron for each wavelength. By substituting Eq.(2.16) from 2.14, n_e is expressed as follows.

$$\Delta N_1 - \Delta N_2 = \left(\frac{e^2}{8\pi^2 c^2 m_e \varepsilon_0} (\lambda_1^2 - \lambda_2^2) \right) n_e \tag{2.17}$$

$$n_e = \frac{\Delta N_1 - \Delta N_2}{(\lambda_1^2 - \lambda_2^2)} \left(\frac{8\pi^2 c^2 m_e \varepsilon_0}{e^2} \right) \tag{2.18}$$

Under the assumption of the singly ionized plasma n_e=n_i, the nutral density distribution is derived from Eqs.(2.14) and (2.18).

$$\begin{aligned} n_n &= n_0 - \frac{\Delta N_1 - (K_i + K_{e1}) n_e}{K_n} && (2.19) \\ n_n &= n_0 - \frac{\Delta N_2 - (K_i + K_{e2}) n_e}{K_n} && (2.20) \end{aligned}$$

Chapter 3

Experimental Apparatus

In this experiment

1. line focused LSD with and without confinement nozzle were visualized by shadowgraph method,
2. 2mm thick LSD was generated and visualized by Mach Zehnder interferometry,

using following apparatus.

3.1 Apparatus for Generating LSD

A 10 J Transversely Excited Atmospheric (TEA) CO_2 pulse laser was used to generate LSD. The laser was line-focused on an aluminum plate to initiate the breakdown in the atmospheric air. An off-axis line-focusing parabolic mirror was used to focus the laser beam. Details of these apparatus and the whole system to generate the LSD are shown in this section.

3.1.1 TEA CO_2 pulse laser

Plasma was produced by Transversely Excited Atmospheric (TEA) CO_2 pulse laser whose nominal energy E_i was 10 J. The laser was made by Usho optical system co. ltd. Its specification is summarized in Table 3.1. Its exterior is shown in Fig.3.1(a). Laser excitation is initiated by triggering the discharge in the gap-switch shown in Fig.3.1(b). The electric circuit is shown schematically in Fig.3.2. Voltage applied to the capacitor is controlled using a slide-regulator, and E_i can be changed slightly using the slide-regulator. E_i also depends on the fill-pressure in the laser-discharge tube. Figure 3.3 shows the relation between E_i and the fill-pressure. E_i increases with the fill-pressure. Pulse energy was measured before and after experiments using a joule-meter; consequent shot-to-shot pulse-energy fluctuations were maintained below 5% throughout experiment.

The laser beam was in the high-order multi-transverse mode: its beam quality factor was approximately 18. Energy distribution of the laser beam was measured using a joule-meter as shown in Fig.3.4. The burn pattern of the laser beam is also shown in the figure. It has gaussian distribution on the horizontal axis, and trapezoidal distribution on the vertical axis. The laser beam cross-section can be approximated by a 30 $\times$30 mm square. Equivalent beam diameter was 34 mm, which was the diameter of a circular beam having the same cross sectional area as the square beam. As in the figure, 20mm height area was used to generate the line focused LSD and that with confinement, while 2mm at the center was used to generate the thin LSD for interferometry.

Pulse shape was measured using a photon-drag detector (Hamamatsu photonics-B749) shown in Fig.3.5. The specification of the detector is summarized in Table 3.2. Typical pulse shape is shown in Fig.3.6. A leading-edge spike appears and an exponentially decaying tail follows. The shape is typical

Table 3.1: Specification of TEA CO_2 lasers.

Product No.	IRL-1201
Max. E_i	10 J
Repetition	single, 0.1∼0.5 Hz
Gas fill pressure	110kPa,a
Impressed voltage	˜10kV
E_i fluctuation	$> \pm 5\%$
Power source	AC 100V 50/60Hz
Laser gas composition	He:N_2:CO_2 = 84:8:8

(a) (b)

Figure 3.1: Picture of TEA CO_2 pulse laser. (a) Exterior of IRL-1201, (b) laser-dixcharge tube and gap-switch.

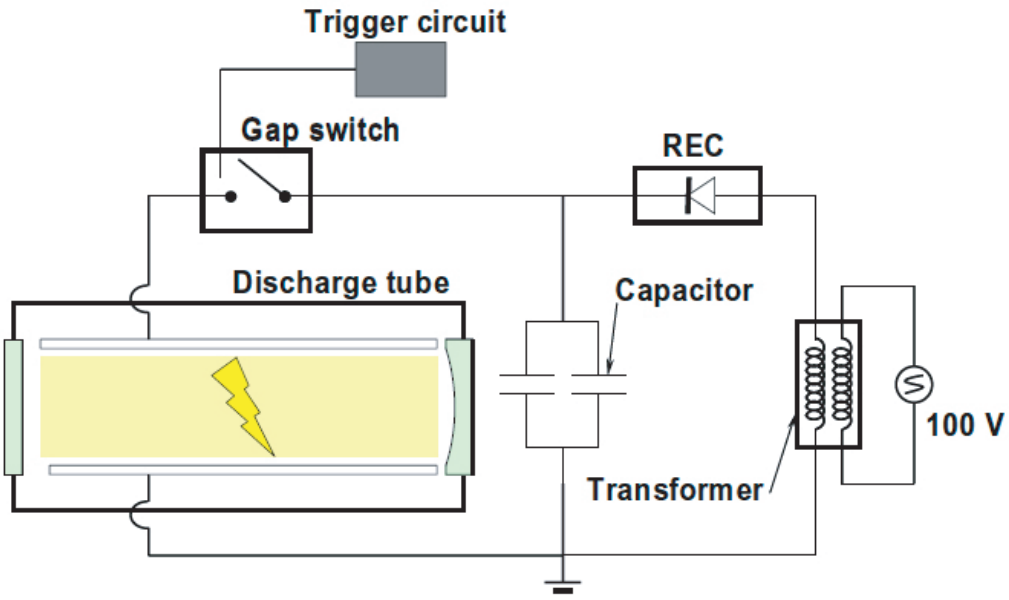

Figure 3.2: Electrical circuit for the TEA CO_2 laser.

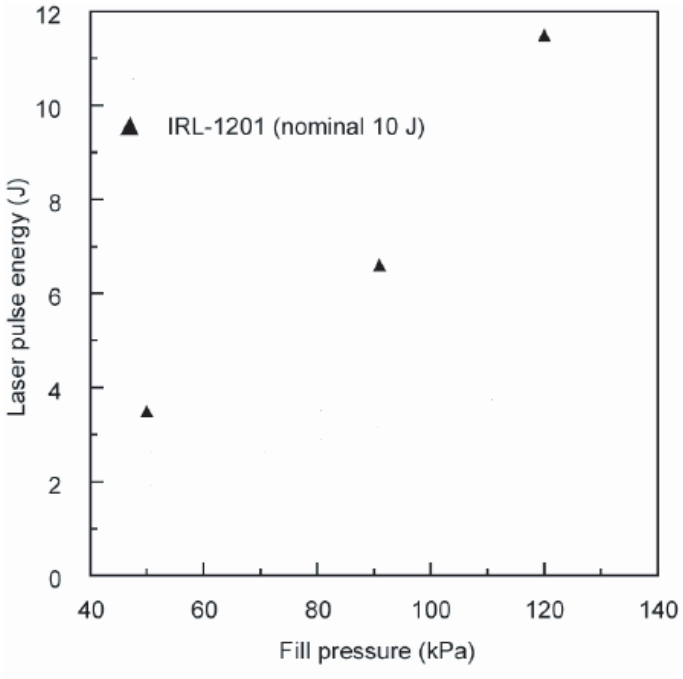

Figure 3.3: Relation between the laser pulse energy and the fill-pressure in the laser-discharge tube.

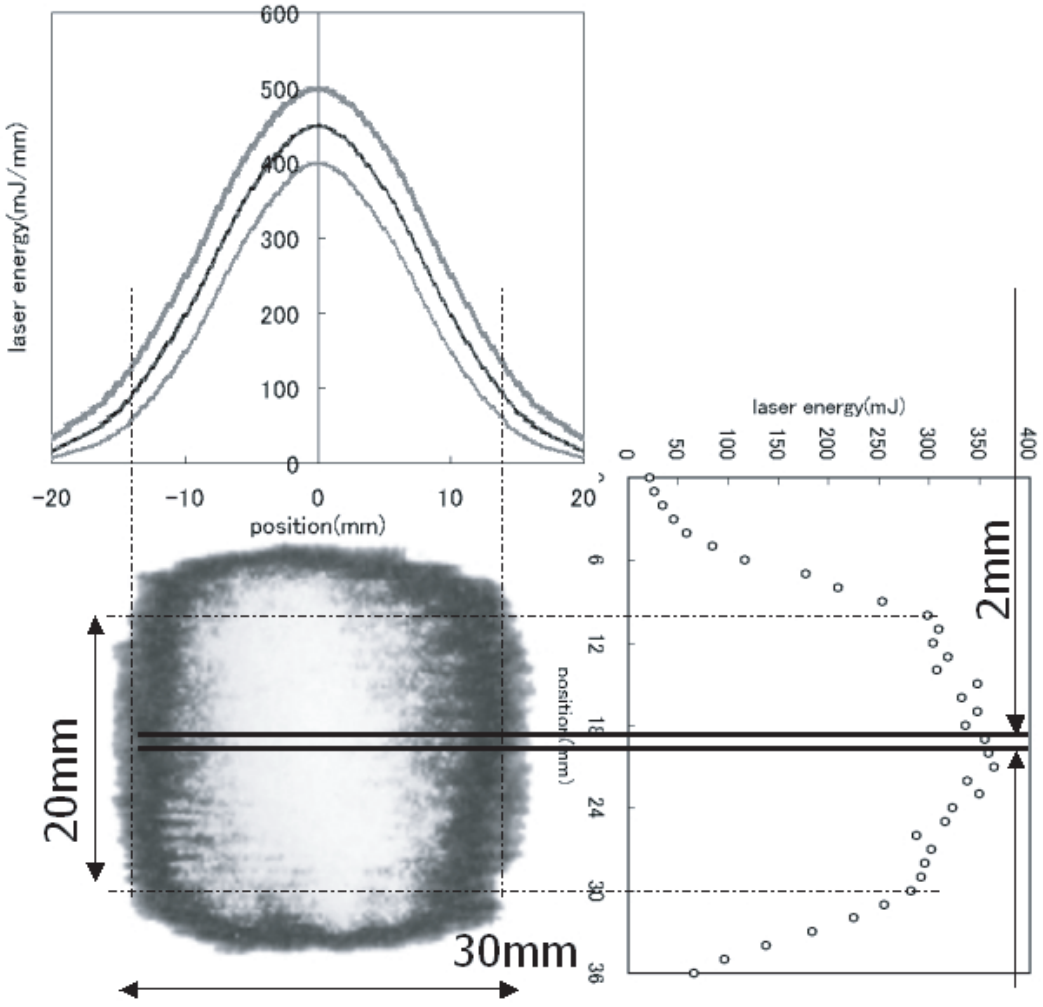

Figure 3.4: Energy distribution of the laser beam.

Figure 3.5: Photon-drag detector.

for TEA CO_2 pulse lasers. FWHM of the spike was 0.12 ± 0.02 μ s. The temporal change in the power at the tail $P_{tail}(t)$ can be approximated as

$$P_{tail}\{t\} = P_{0,tail} \exp\left(-\frac{t}{\tau_d}\right) \tag{3.1}$$

The pulse shape is influenced by the fill pressure in the discharge tube. Figure 3.7 shows the relation between the laser pulse shape and the fill-pressure in the laser discharge tube. The decay-constant of the tail τ_d decreases with the fill-pressure. The duration of the laser irradiation is mostly proportional to the duration of the excitation discharge, which is presumed to decrease with the fill-pressure of the gas in the tube. At the fill-pressure lower than 50 kPa, the reproducibility of the laser pulse shape became quite poor due to the instability of the excitation discharge in the tube. Tests were performed at the fill-pressure lower than 120 kPa for the safety of the discharge tube. With the nominal fill pressure at 110 kPa, the tail decay-constant τ_d was 1.15 ± 0.05 μs. The fraction of $E_{\rm i}$ that is contained in the tail was approximately 75 %.

Table 3.2: Specification of Photon-drag detector(Hamamatsu photonics, B749).

Aperture diameter	5mm
Sensitivity	1.2 V/MW
Rise time (10∼90%)	$<$ 1 ns

3.1.2 An off-axis line-focusing parabolic mirror

The laser beam was focused using an off-axis line-focusing parabolic mirror that was free from aberration. The schematic of the mirror is shown in Fig.3.8. Its focal lengths was 48 mm along the optical axis; its corresponding focusing f-number was 1.5. (Here, "corresponding f-number" is defined as laser focal length / laser beam width.) It reflects an incident laser beam by 90 degrees along the optical axis into focus. Line width on the focus was estimated at 0.25 mm.

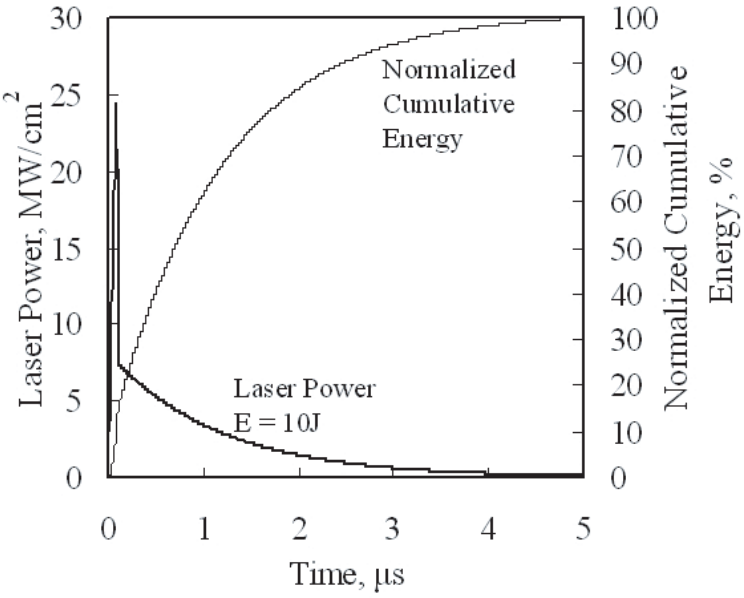

Figure 3.6: Laser pulse shape typical for IRL-1201.

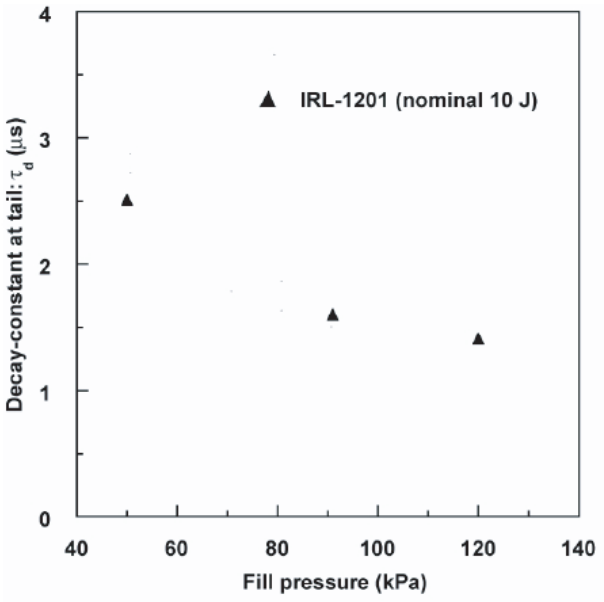

Figure 3.7: Relation between the decay-constant at the exponentially-decaying tail and the fill-pressure in the laser-discharge tube.

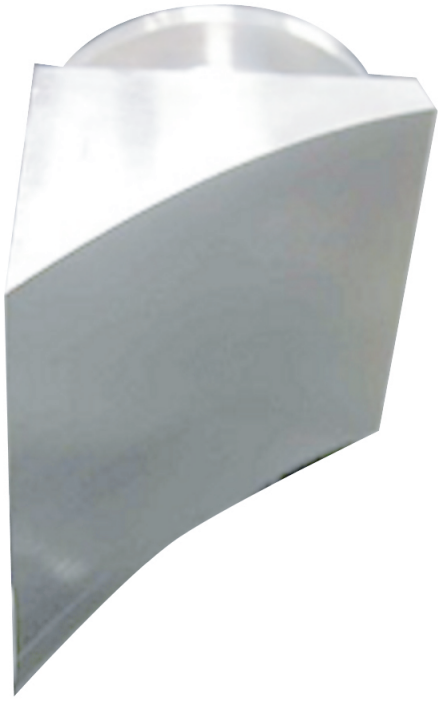

Figure 3.8: The schematic of the off-axis line-focusing parabolic mirror.

3.1.3 Aluminum plate apparatus for breakdown initiation and blast wave confinement

The laser was line-focused on an aluminum plate to initiate the breakdown in the atmospheric air. Ablation of the aluminum was not expected here.

As seen in Fig.3.9, two glass walls were attached perpendicularly to the aluminum plate, and the LSD was confined into 20mm height space for the investigation of the line focused LSD and that with a confinement nozzle. The apex angle of the nozzle was set slightly smaller than that of the focusing laser channel. For Mach Zehnder interferometry, the LSD was generated in 2mm height space in order to modify the strong refractive effect, as seen in Fig.3.10.

3.2 Apparatus for imaging the LSD

Parallel beam from the light source passed through the shadowgraph apparatus or Mach Zehnder interferometer, and the image was taken by an Image-intensified Charged Couple Device (ICCD) camera. Details of these apparatus and the whole system to generate the LSD are shown in this section.

3.2.1 Light Source

A He-Ne laser and a diode pumped green laser were used as a light source of visualization. These lasers were combined using a red-reflector (Thorlabs, Inc.), which transmits the 532nm(green) light while reflecting the 633nm(red) light. Its dependence property of the reflectance ratio on the wavelength is shown in Fig.3.11. Combined laser was focused to the pinhole by the objective lens, and dirty spatial profile was collimated to be clean. (This apparatus is called spatial filter.) Clean profiled light from spatial filter, was parallelized by another lens. As a laser was used for the light source, its high

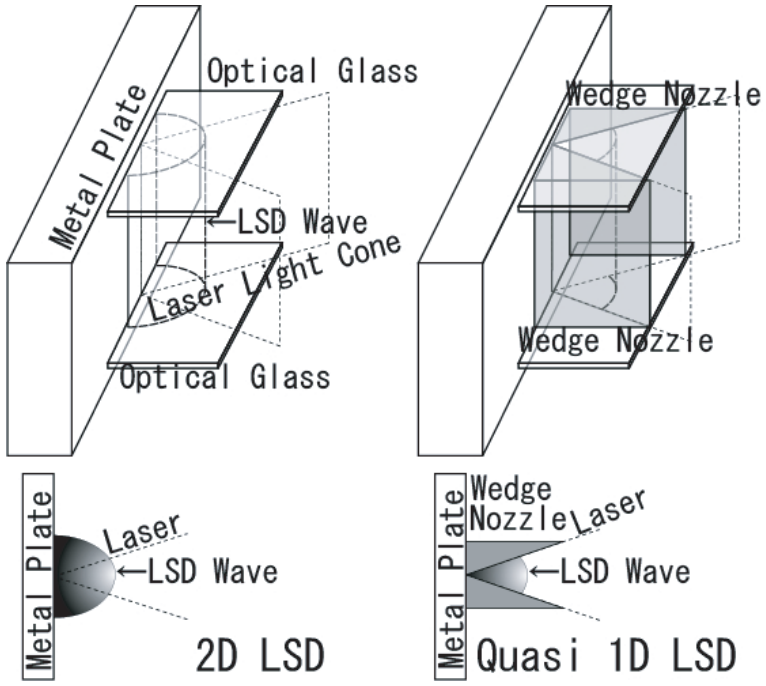

Figure 3.9: The schematic of the aluminum plate apparatus, used to initiate the LSD and to confine the blastwave.

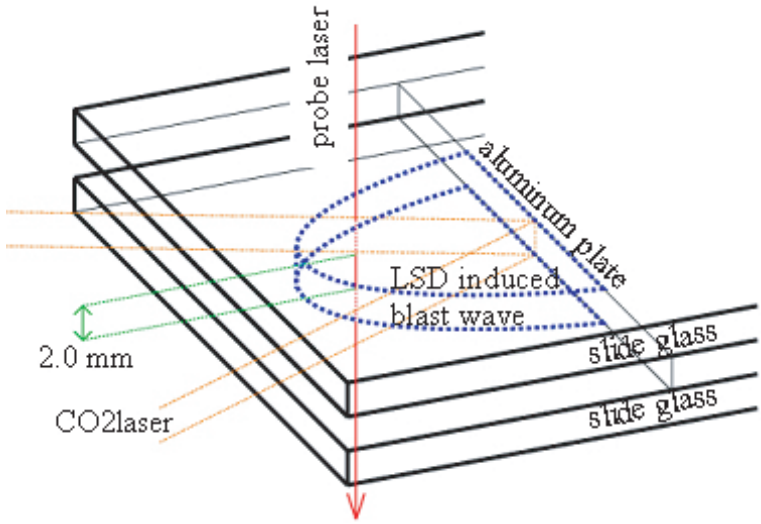

Figure 3.10: The schematic of the aluminum plate apparatus for Mach Zehnder interferometry.

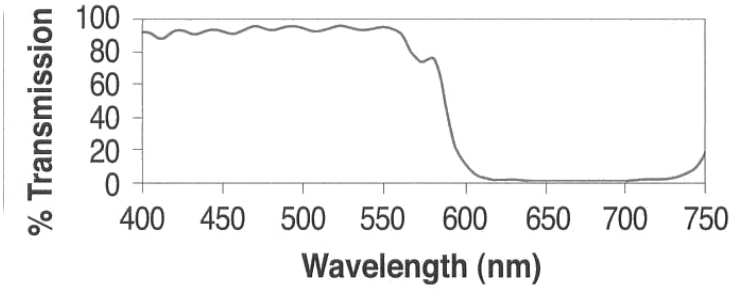

Figure 3.11: Red-reflector's dependence property of the reflectance ratio on the wavelength.

Figure 3.12: InstaSpecV^{TM} ICCD detector.

coherency produced a obstructive fringe pattern (which was like a Newton ring), by the interference of the transmitted laser light and the reflected laser light of the objective lens.

3.2.2 ICCD camera

The shadowgraphs and Mach Zehnder interferograms were taken using an ICCD camera (Oriel Instruments InstaSpecV^{TM} ICCD detector, Model 77193-5) shown in Fig.3.12. It's dependence of the quantum efficiency on the wavelength is shown in Fig.3.13. The camera image intensifier was operated as a shutter and an optical emission from the gap-switch of the laser discharge tube was used to trigger the shutter: strong emission from the gap-switch prior to laser oscillation was detected by a photo-sensor through an optical fiber. The measurement sequence is shown in Fig. 3.14. Soon after the gap-switch was triggered, its emission was initiated to trigger the measurement system. The laser irradiation started about 200 ns after the gap-switch ignition. The photo-sensor signal was transmitted to a delay-circuit (Stanford Research Systems, Inc., Digital Delay/Pulse Generator Model DG535), which allowed the setting of a delay period from the beginning of the laser pulse. The whole imaging set-up is shown with the shodowgraph system in Fig.3.15.

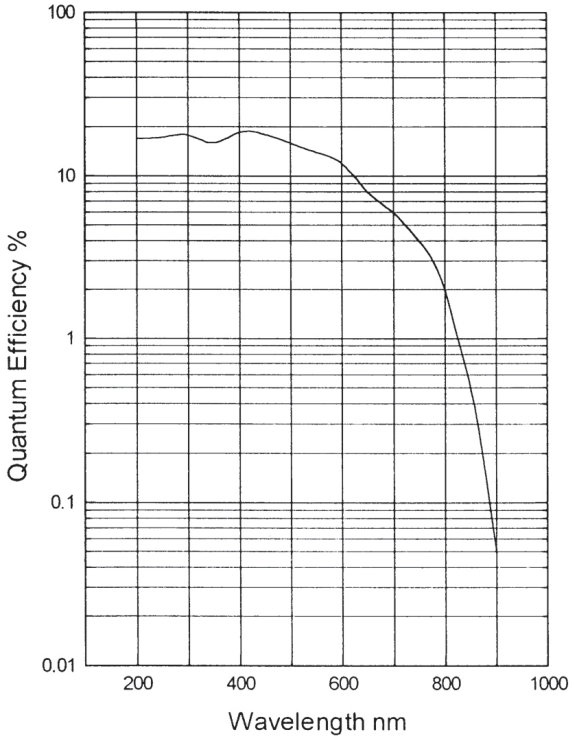

Figure 3.13: Typical quantum efficiency versus wavelength.

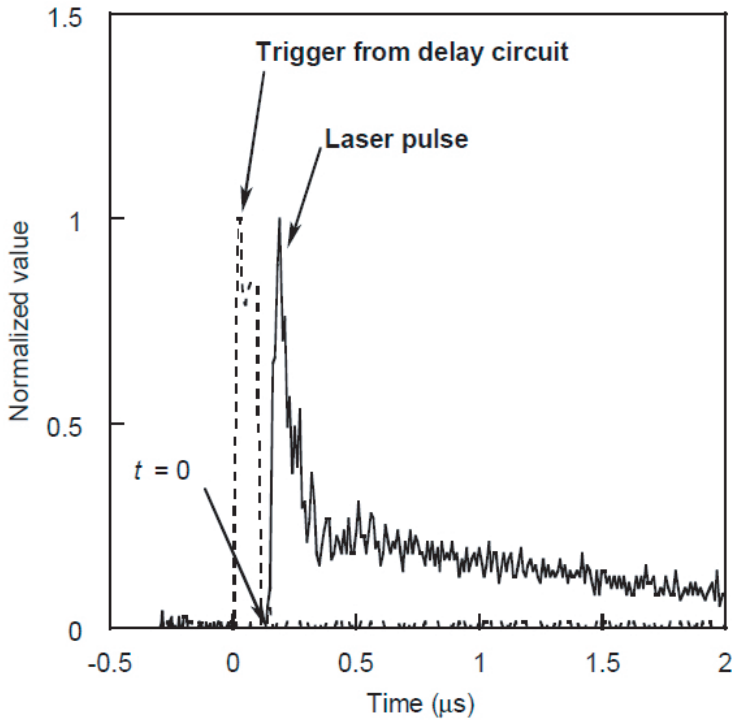

Figure 3.14: Measurement sequence: the laser pulse was measured using a photon-drag detector.

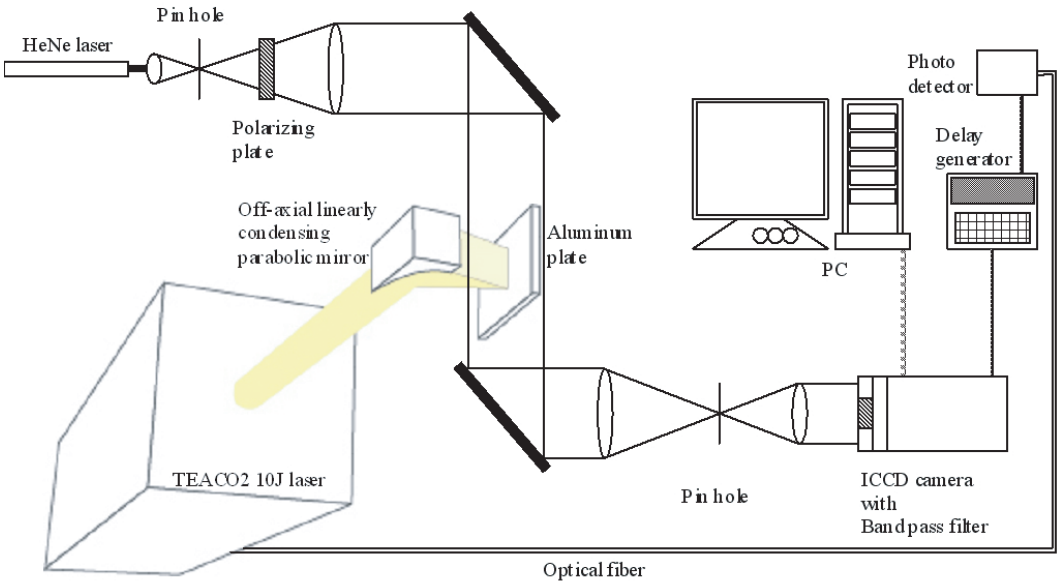

Figure 3.15: Imaging setup.

3.2.3 Two-wave Mach Zehnder interferometer

The whole system of two-wave Mach Zehnder interferometer is shown in Fig.3.16. The detail of the optical equipments used in this system, is listed in Table 3.3. The Pin-hole.2 and the Filter.1 and 2 were used to remove the strong emission by the plasma. As in the table, width and height of the pinhole was different. This is due to the following effect. When the pinhole diameter was small enough ($<$10mm), diffractive effect becomes unignorable. The probe laser diffracts prominently, especially when the phase of the probe laser was perturbed in the phenomena. The direction of the perturbation is dependent on the direction of the density gradient in the phenomena. On the contrary when the pinhole diameter is large ($>$4mm), plasma emission cannot be removed. Therefore, pin-hole width was set in order to remove the plasma emission sacrificing the clear interferogram in this direction, and height was set to visualize the phenomena without the disturbance of the diffractive effect in the direction of the target density distribution.

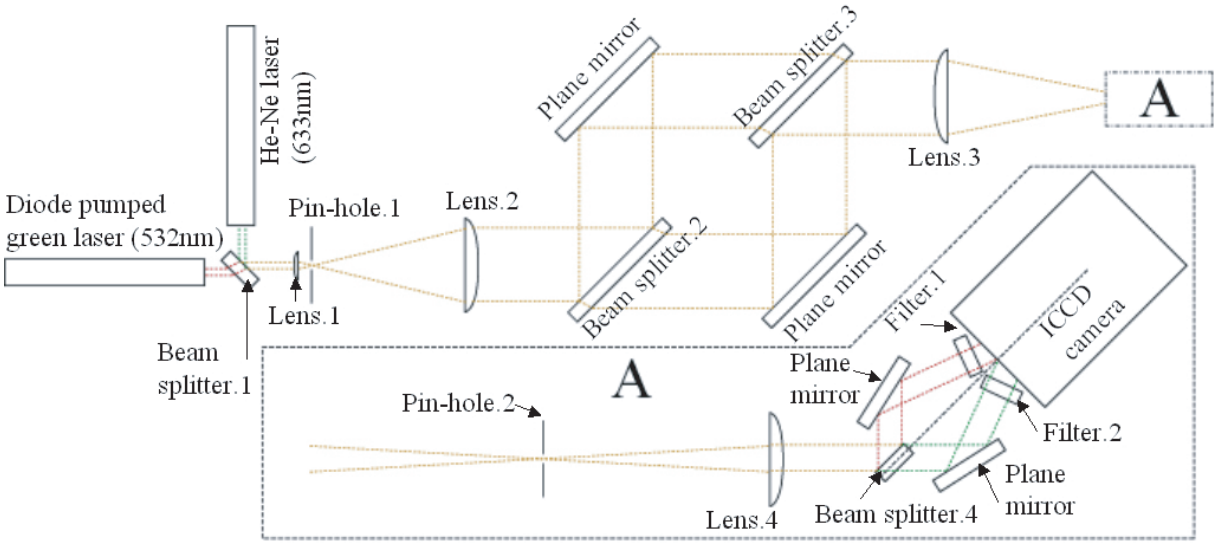

Figure 3.16: The whole system of two-wave Mach Zehnder interferometer.

Table 3.3: Specification of optical equipments.

	Note
Pin-hole.1	ϕ=10[μm], 50MW/cm^2
Pin-hole.2	3mm width, 12mm hight
Lens.1	f=15[mm]
Lens.2	f=[mm]
Lens.3	f=[mm]
Lens.4	f=[mm]
Beam splitter.1	Red reflector(Thorlabs)
Beam splitter.2	1:1
Beam splitter.3	1:1
Beam splitter.4	Red reflector(Thorlabs)
Filter.1	Band-path filter, λ=633$\pm$1nm
Filter.2	Band-path filter, λ=532$\pm$1nm

Chapter 4

Results and Discussions

4.1 Line focused LSD with and without confinement

Figure 4.1 shows the shadowgraphs of a line focused LSD, and Fig.4.2 shows that with nozzle confinement. In these figures, laser started to irradiate at t=0μs. Figure 4.3 shows temporal variation of the shock and plasma front displacements on the laser axis. As seen in the figure, the shock front and plasma front began to separate at 1.3μs for the line focused LSD and 1.8μs for that with confinement.

4.1.1 Calculation of blast wave efficiency

The blast wave energy E_{BW} was deduced from the observed shock propagation characteristics using the self-similar equation.[28] According to the self-similar equation of a cylindrical blast wave,[29] time varying radius $r_{\mathrm{s}}(t)$ initiated at t=0 is expressed as

$$r_{\mathrm{s}}(t) = \zeta_0 \left(\frac{E_{\mathrm{BW}}/(\alpha/2\pi)}{\rho_{\mathrm{a}}} \right)^{\frac{1}{4}} t^{\frac{1}{2}} \tag{4.1}$$

where ζ_0 is a function of γ and its value is 1.00 for γ = 1.4. ρ_{a} is the ambient density (=1.28[kg/m^3]) and α is the apex angle of the blast wave expansion area; $\alpha = \pi$ for simple line focus case, and 0.24 rad for nozzle confinement case. Although the self-similar solution is inaccurate for intermediate shock strengths, it is still a good approximation for when M_{s} is at 2 - 3 according to the comparison with a perturbation solution for a cylindrical blast wave.[30] On the contrary, calorically perfect gas assumption (γ=const, then ζ_0=const) is valid approximately for M_{s}<4 in the 1atm air according to the comparison of the analysis of blast wave in perfect gas with that in real gas.[31] Rewriting Eq.(4.1), the blast wave area S_{BW} is expressed as a linear function of time as,

$$S_{\mathrm{BW}} = \frac{\alpha}{2} r_{\mathrm{s}}^2 = \frac{\alpha}{2} \zeta_0^2 \sqrt[2]{\frac{2\pi E_{\mathrm{BW}}}{\alpha \rho_{\mathrm{a}}}} (t - t_0) \equiv A(t - t_0) \tag{4.2}$$

where A is a proportional constant and t_0 is the experimental time-lag from an ideal line source expansion. This equation can be applied even to an elliptical expansion cases as seen in Fig.4.1, by the Kompaneets approximation.[32] Thus the blast wave energy was calculated. After the LSD has terminated, laser energy cannot drive the shock wave because LSC heating becomes almost adiabatic. Therefore, energy input to the blast wave is terminated when the LSD has terminated. E_{BW} was calculated from the inclination of $S_{\mathrm{BW}}(t)$ for M_{s}<5 as shown in Fig.4.4.

The blast wave energy efficiency η_{BW} was calculated as

$$\eta_{\mathrm{BW}} = \frac{E_{\mathrm{BW}}}{E_{\mathrm{i}}} \tag{4.3}$$

where E_{i} is the irradiated laser energy.

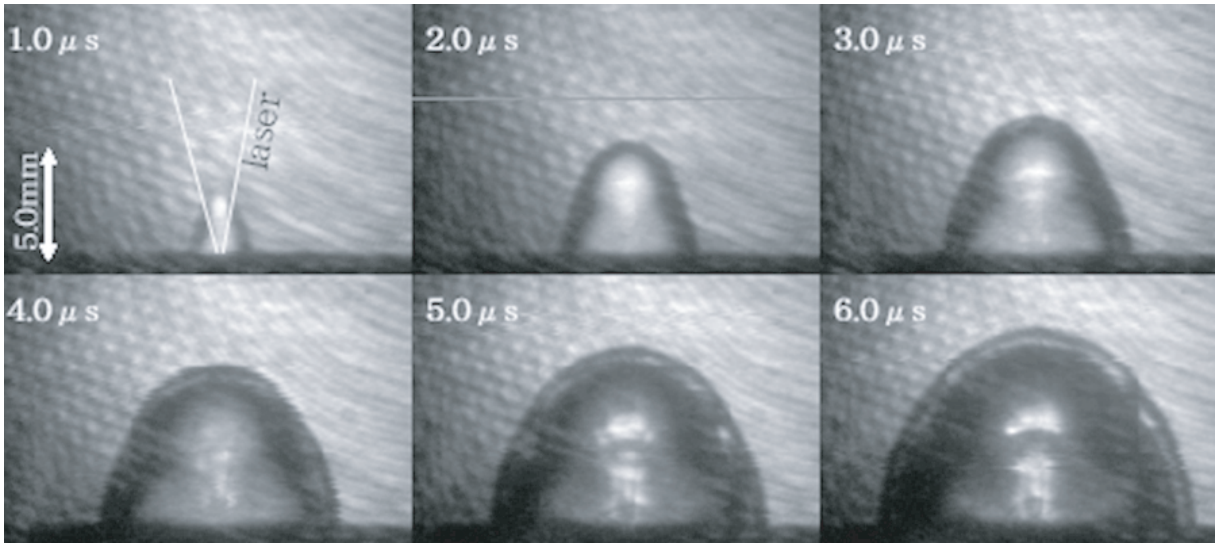

Figure 4.1: Shadowgraphs of the evolution of line focused LSD wave.

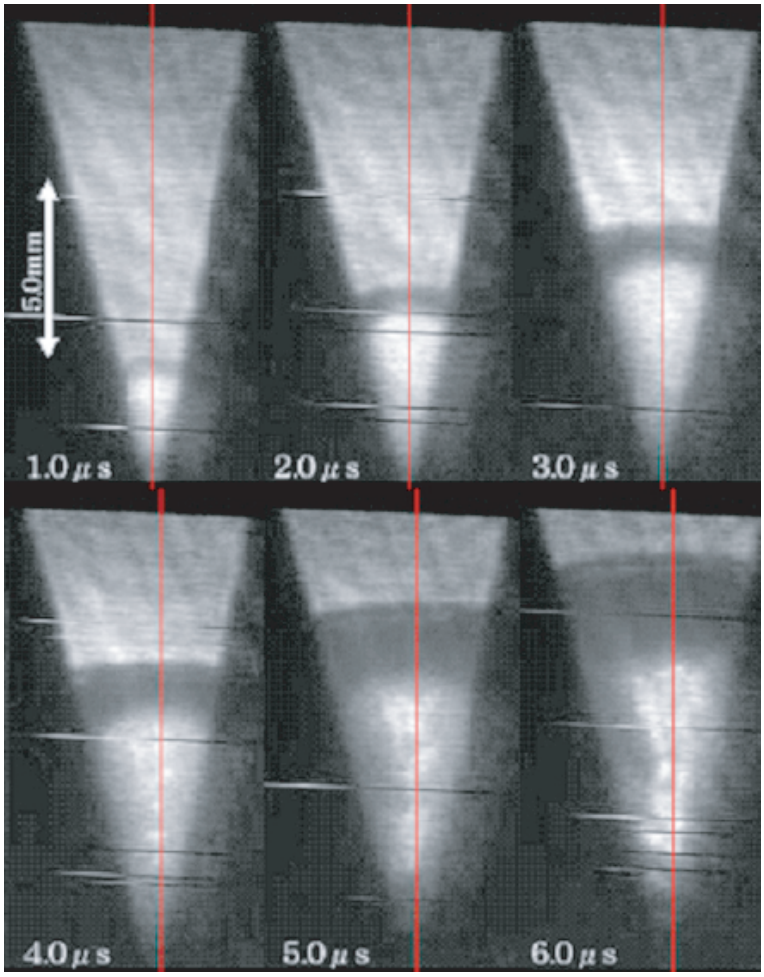

Figure 4.2: Shadowgraphs of the evolution of line focused LSD wave with nozzle shaped confinement.

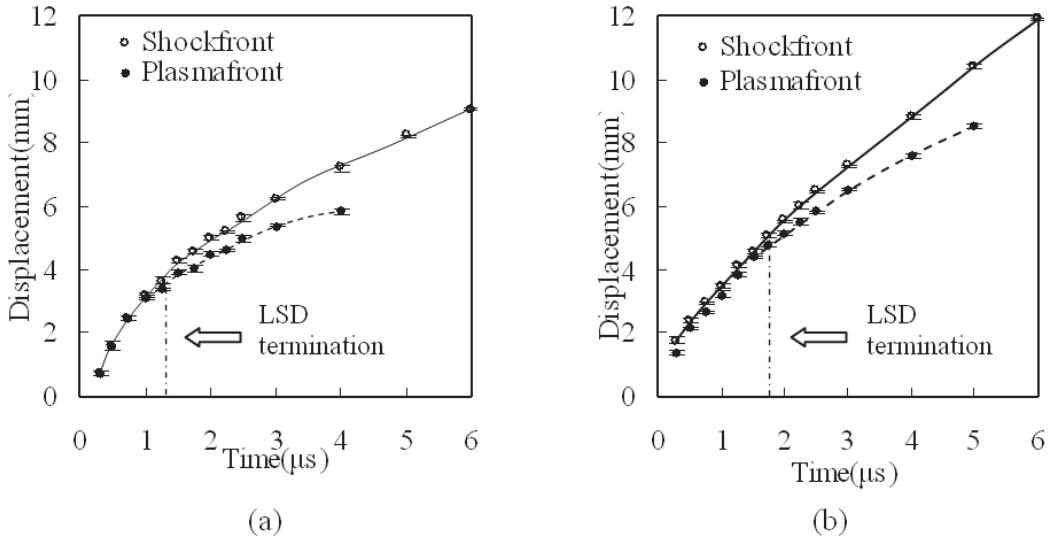

Figure 4.3: Displacements of the shock and plasma front of the line focused LSD(a) and that with confinement(b).

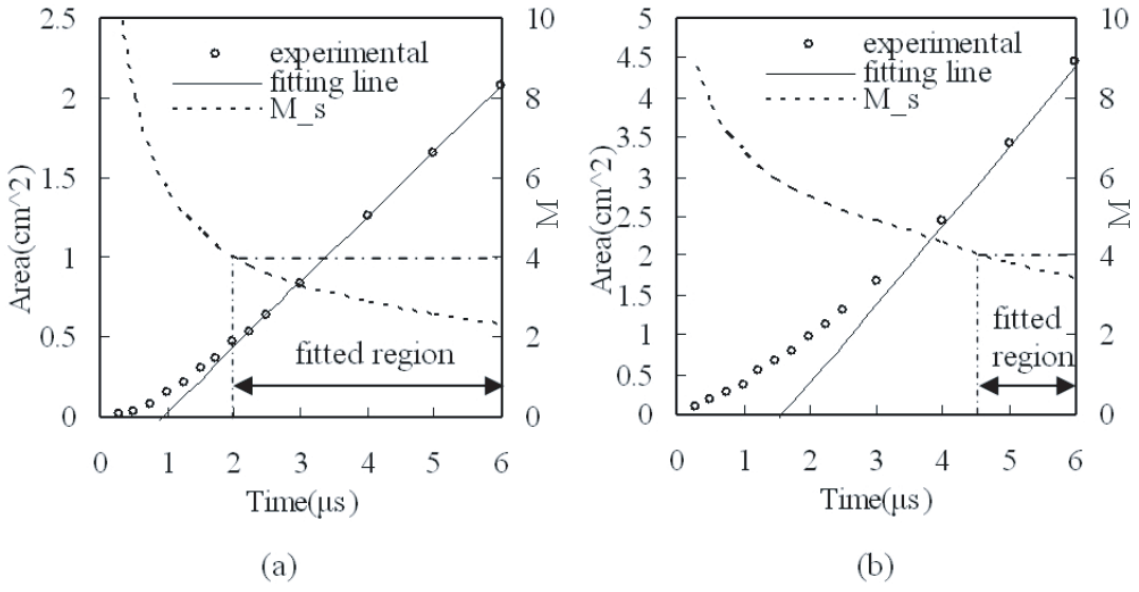

Figure 4.4: Temporal variation of the blast wave area $S_{\mathrm{BW}}(t)$ and shock propagation Mach number M_{s} for the line focused LSD(a) and that with confinement(b).

4.1.2 Effect of line focus and confinement

In Table 4.1, deduced η_{BW} are listed along with the LSD termination conditions, such as the termination time t_{LSD}, laser intensity threshold S_{LSD} and Mach numbers M_{LSD}. In the line focused cases, the LSD terminated earlier than point focused cases because of the lower laser intensity on the LSD wave front, resulting in the lower η_{BW}. However, S_{LSD} in the line focused LSD with confinement was apparently lower than the other cases.

Table 4.1: η_{BW}, and LSD Termination Conditions.

Dimension Of Phenomena	**Line**	**Nozzle**	**Point**	
Focal Length / Beam Diameter	1.5	2.0	1.1	2.2
η_{BW}[%]	33	37	41	44
$t_{\mathrm{LSD}}[\mu\mathrm{s}]$	1.2	1.8	2.2	2.5
$S_{\mathrm{LSD}}[\mathrm{MW/cm^2}]$	3.4	1.7	2.6	3.7
M_{LSD}	5.3	6.3	5.3	5.4

Fractional laser absorption η_{LSD} and η_{BW} are listed in Table 4.2 . As seen in the table, η_{BW} is proportional to η_{BW} for all cases. Therefore, the decrease in η_{BW} can be attributed to that in η_{LSD}. This also indicates that reduction in radiation and frozen flow losses by decreasing the peak laser intensity in the vicinity of focal line was not appreciable in this range of energy. However, S_{LSD} in the confined LSD was apparently lower than those in other cases as seen in Table 4.1. Therefore, there is a possibility to have high η_{LSD} in LSD confinement configuration by optimizing the matching of the laser pulse shape and variation of the laser cross section.

Table 4.2: η_{LSD} and η_{BW}.

Dimension Of Phenomena	**Line**	**Nozzle**	**Point**	
Focal Length / Beam Diameter	1.5	2.0	1.1	2.2
η_{BW}[%]	33	37	41	44
η_{LSD}[%]	68	81	89	90
$\eta_{\mathrm{BW}}/\eta_{\mathrm{LSD}}$[%]	49	47	46	49

4.2 Mach Zehnder interferogram

Figures 4.5, 4.6 4.7 shows the Mach Zehnder interferograms (for 633nm and 532nm and shadowgraph images of a line focused 2mm thick LSD. In these figures, the laser started to irradiate at t=0ms. As seen in Fig.4.8, temporal variation of the shock front displacement for the 2mm thick LSD was almost the same as that for the 20mm thick case.

4.2.1 Methods to extract the electron and neutral number densities

The variance of the brightness on the center axis was extracted from the visualized data of LSD, as Fig.4.9. Local shift of the fringe pattern was digitalized by detecting the peaks of contrast in this data as seen in the figure.

With no flow in the test section, these peaks line evenly. This average interval h_0 could be measured from Mach Zehnder interferogram with no flow in the test section. By defining the position of nth peak

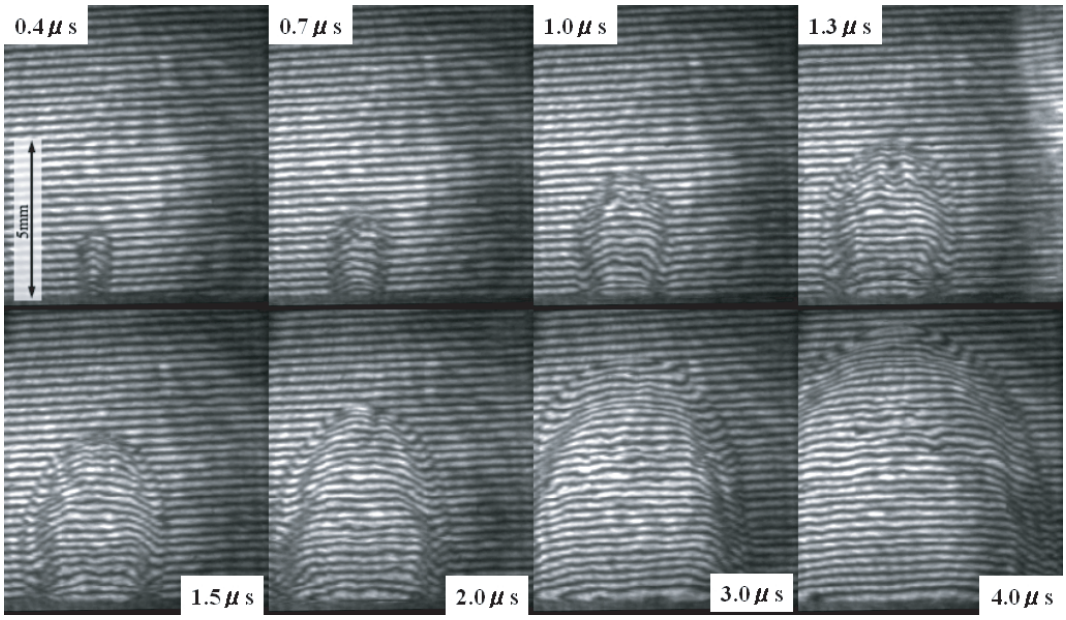

Figure 4.5: Mach Zehnder interferograms of the line focused 2mm thick LSD (for 633nm).

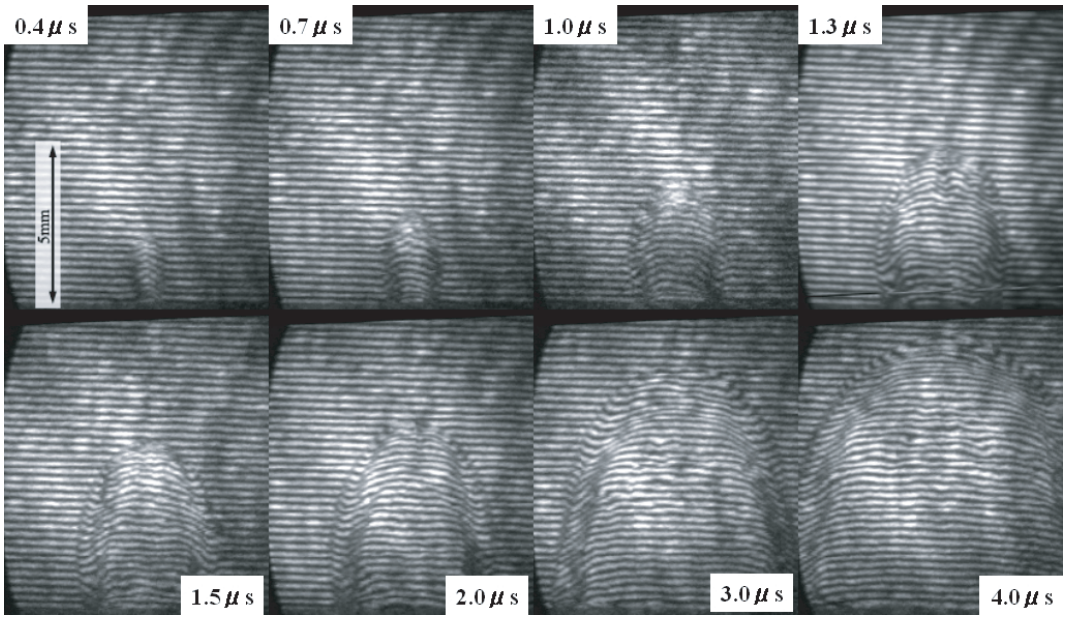

Figure 4.6: Mach Zehnder interferograms of the line focused 2mm thick LSD (for 532nm).

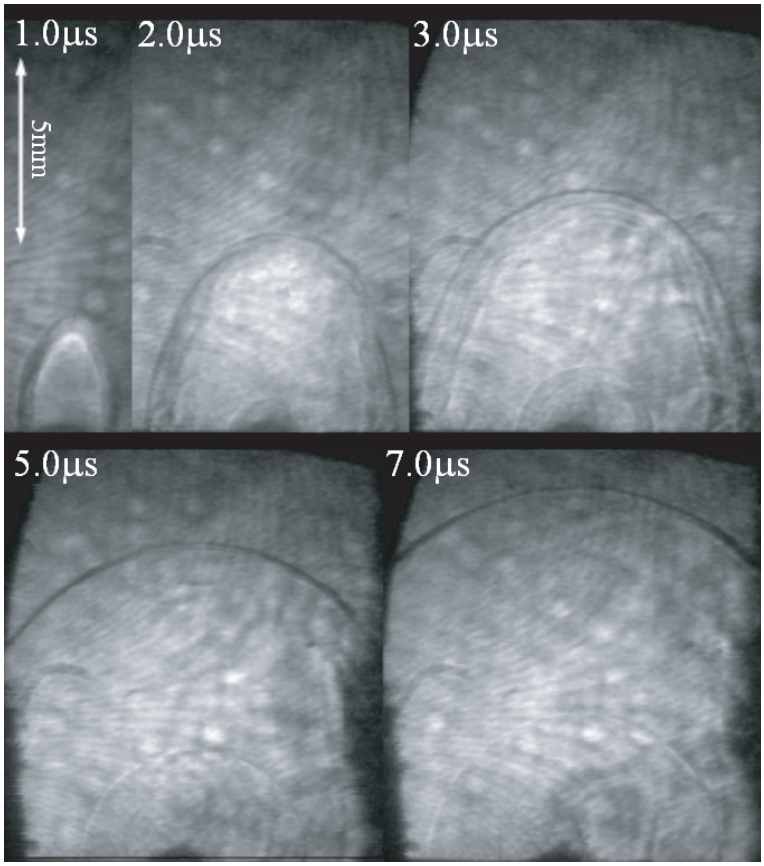

Figure 4.7: Shadowgraph images of line focused 2mm thick LSD.

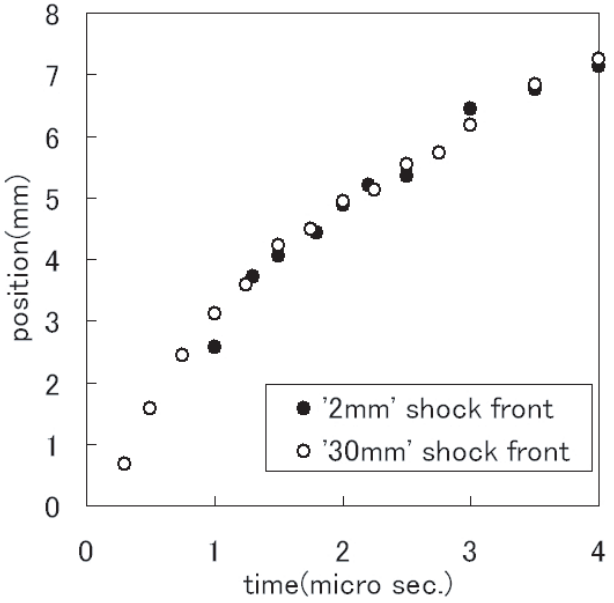

Figure 4.8: Temporal variation of the shock front displacement for 2mm and 20mm thick LSD.

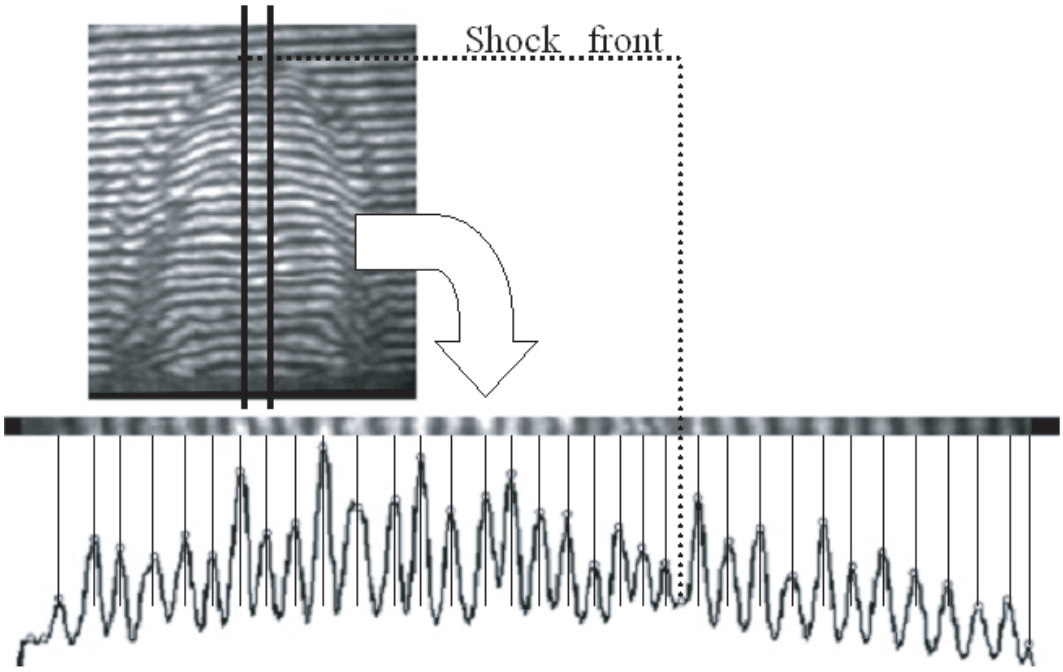

Figure 4.9: The variance of the brightness on the center axis.

from the peak of baseline as x_n, movement of the each peak could be determined. This movement could be expressed on the number of fringe shift basis, $h(x_n)$ as follows.

$$h(x_n) = x_n - h_0 n \tag{4.4}$$

This is shown in Fig.4.10. In this figure, the baseline is set to wall and the positive shift indicates the shift toward the wall. The shift right after the shock front is invisible due to the strong stand up of the density. Therefore, the visible information indicates the trailing edge of the high density of electron or neutral. From Eq.(2.3), the difference of the refractive index ΔN is expressed as follows.

$$\Delta N(x_n) = \frac{h(x_n)\lambda}{d} \tag{4.5}$$

This ΔN is the difference in refractive index from the baseline area, which is slightly different from Eq.(2.3) where ΔN was the difference of the refractive index between the reference area and the object. This is caused by the invisible fringe shift at the shock front. However, the variation of the refractive index inside the blast wave is exactly the same without the information at the shock front. Therefore by the appropriate assumption of the absolute value at somewhere inside the blast wave, whole density distribution of electron and neutral would be known. This is explained next. In this experiment, ΔN_{red} and $\Delta N_{\mathrm{green}}$ for two-wavelength $\lambda_{\mathrm{red}}(= 633nm)$ and $\lambda_{\mathrm{green}}(= 532nm)$ were acquired from each interferogram. This is shown in Fig.4.11. And the amplitude variation of the difference in these value indicates the electron density distribution. In this figure, baseline of the difference was set to the end of trailing age(that is about 1.7mm from the wall) assuming that the electron density around there was smaller than the detection range, which was about 0.6×10^{24}. (Detection range was assumed by the analysis of no flow interferogram as seen in Fig.4.12). Neutral density was calculated as well. Results of these calculation are shown in Fig.4.13. Some characteristics, such as peak number density, peak position, characteristic length of the density distribution were measured as seen in the figure. The characteristic length was estimated by fitting the density distribution by an exponential function. These characteristics are summarized in the next section.

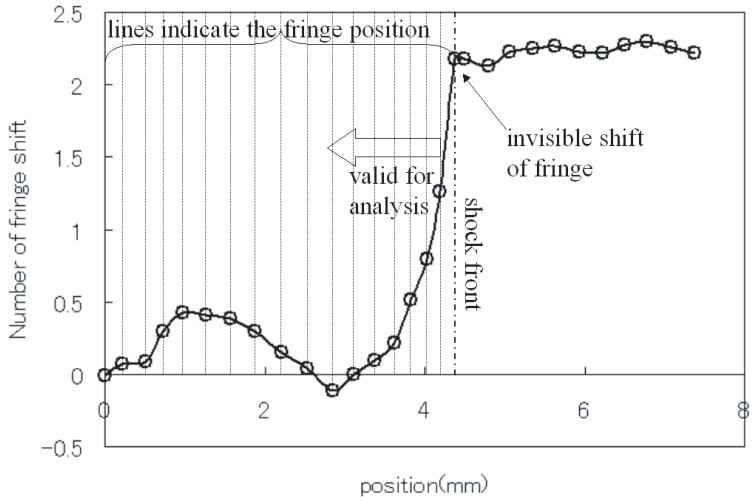

Figure 4.10: The movement of the each peak on the axis.

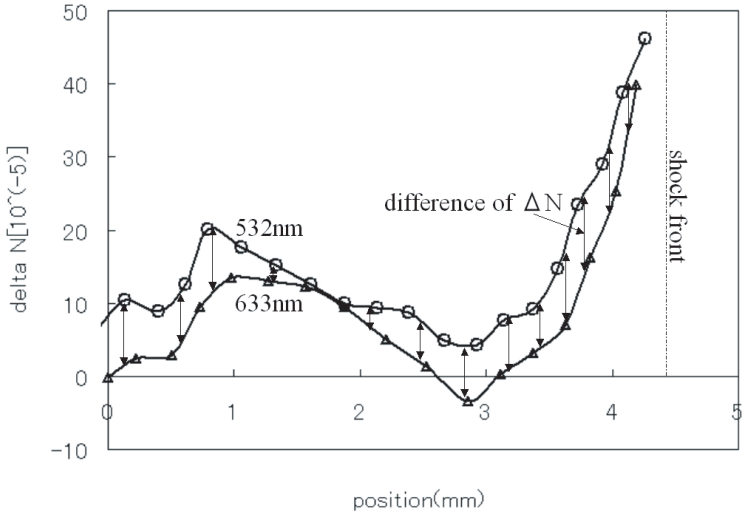

Figure 4.11: Δ N_{red} and Δ N_{green}.

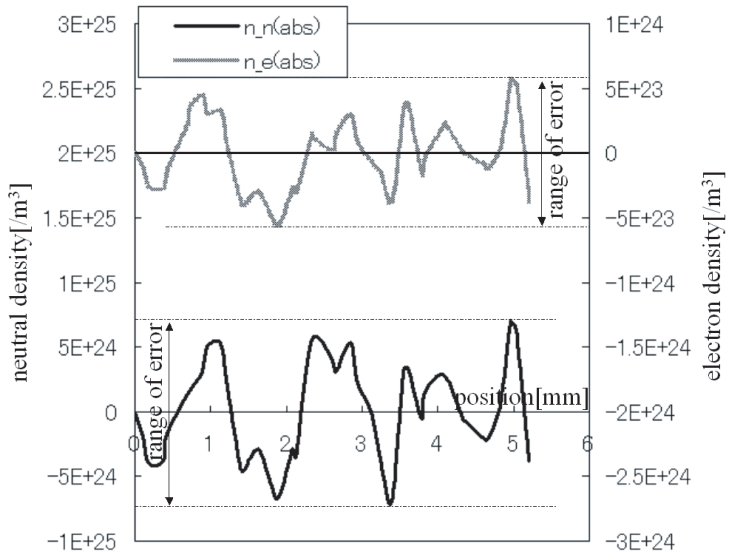

Figure 4.12: The analysis of the no flow interferogram, which was used to determine the detection range.

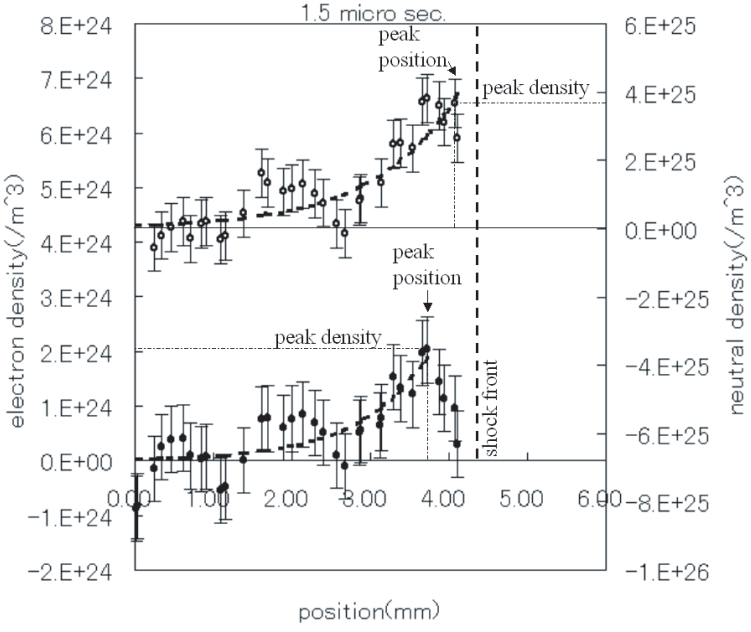

Figure 4.13: Electron and neutral number density extracted from the two wave interferogram.

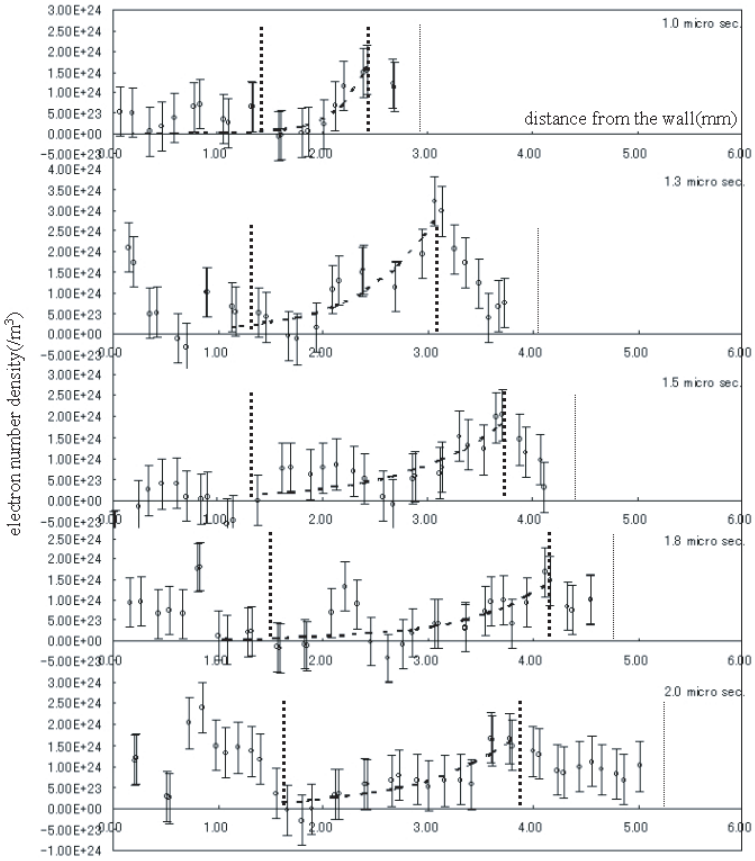

Figure 4.14: Temporal variation of the electron number density distribution.

4.2.2 Results of analysis

Figure 4.14 shows the temporal variation of the electron number density distribution, and it's fitting line.

Figure 4.15 shows the temporal variation of the peak position for the electron and neutral number density. As seen in the figure, peaks of the electron and neutral density disgregate around 1.5 μs because of the LSD termination. This is similar to the results of LSD termination for the line focused 20mm thick LSD (which was around 1.3 μs).

4.2.3 The absorption length and LSD termination

In LSD region, 1.0×10^{24} order electron density may not exist without the support of laser energy irradiation, due to the fast recombination. Therefore, characteristic length of the electron density distribution could be associated to the laser absorption length. Thus laser absorption length l is defined as, in this analysis, the distance from the shock front, where the electron number density becomes $1/e$ of the peak, is recognized as the absorption length.

As mentioned before, Raizer predicted the LSD termination theshold absorption length as

$$l = 4r \tag{4.6}$$

Figure 4.16 shows the temporal variation of the LSD termination theshold absorption length and the absorption length of the observed line focused LSD.

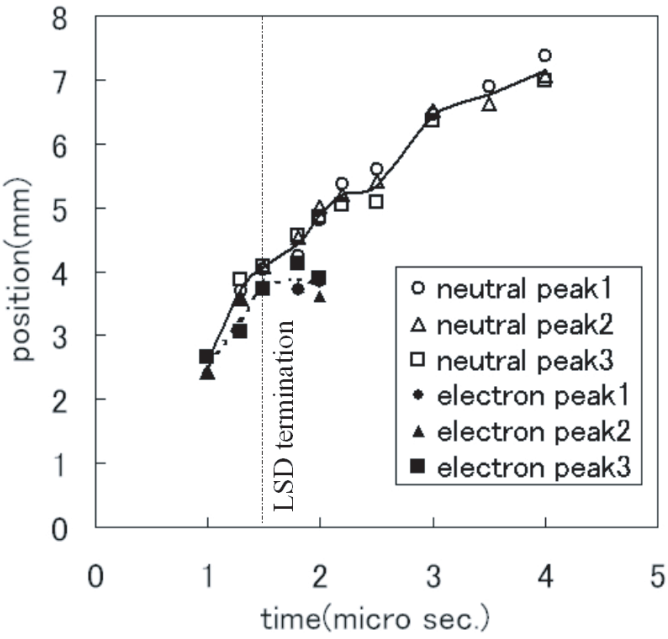

Figure 4.15: Temporal variation of the characteristic length of electron density distribution.

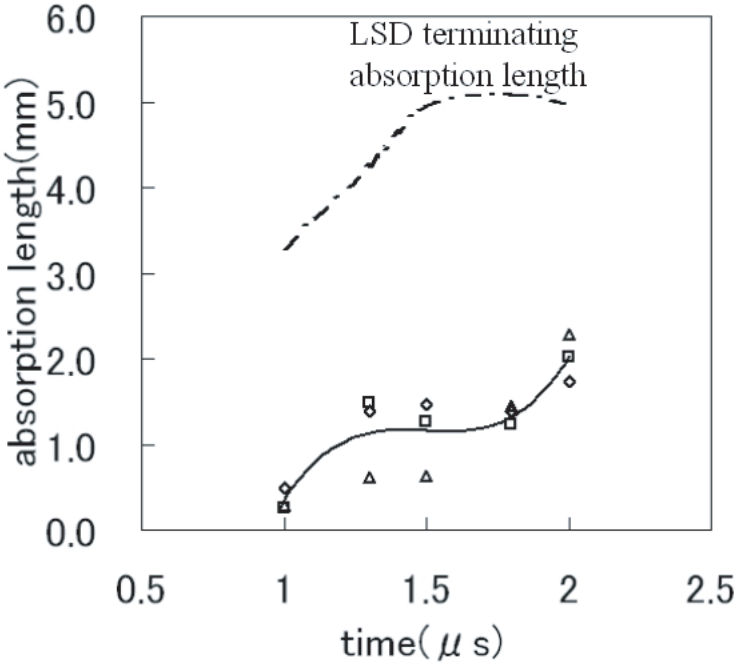

Figure 4.16: Temporal variation of the absorption length of line focused LSD.

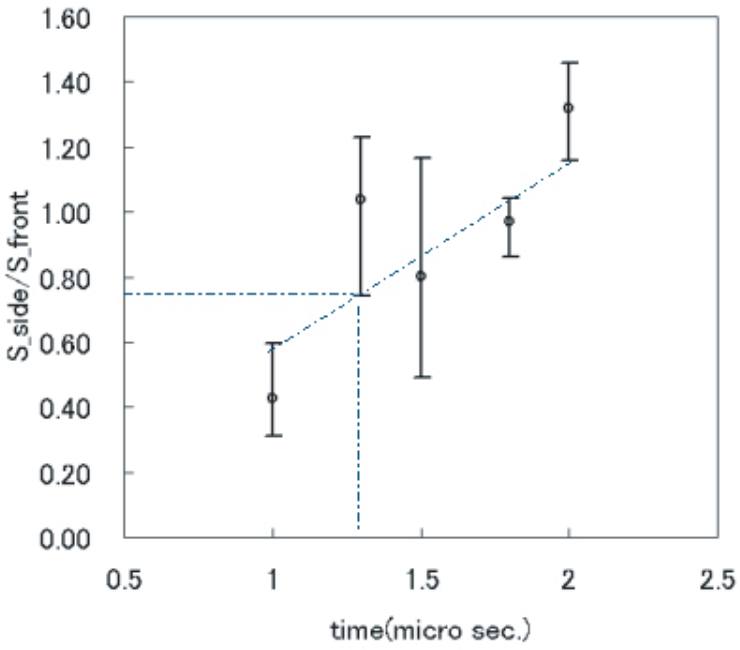

Figure 4.17: The ratio of the $S_{\rm side}/S_{\rm front}$ at the LSD termination.

In Fig.4.17, ratio of the $S_{\rm side}/S_{\rm front}$ at the LSD termination is shown. It was estimated to be 0.8±0.4 in this experiment, which was much smaller than the Raizer's prediction, $S_{\rm side}/S_{\rm front} \approx 8$. This difference may be due to the difference of the laser light channel geometry, which was one demensional in Raizer's theory, while it was focused in this experiment.

Chapter 5

Conclusions

1. The line focused LSD was terminated earlier than the point focused case because of lower laser intensity on the LSD wave, resulting in lower fractional laser absorption. The blast wave energy efficiency was proportional to the fractional laser absorption for all cases. This indicates that reduction in radiation and frozen flow losses by decreasing the peak laser intensity was not appreciable in this range of energy.

2. In the line focused LSD with confinement, the LSD threshold laser intensity was apparently lower than those in other cases. Therefore, there is a possibility to have high fractional laser absorption in LSD confinement configuration by optimizing the matching of the laser pulse shape and variation of the laser cross section along the laser channel.

3. Electron and neutral number density in the LSD region were acquired. Absorption length of the laser in the LSD region was estimated by the electron number density distribution, and the LSD terminating $S_{\mathrm{side}}/S_{\mathrm{front}}$ was estimated to be 0.8 ± 0.4 which was smaller than the Raizer's prediction which was 8.

Bibliography

[1] Kantrovitz, A. "Propulsion to Orbit by Ground Based Lasers," *Aeronautics and Astronautics*, vol.10, 1972, pp. 74-76.

[2] Hettche, L. R., Schriempf, J. T., and Stegman, R. L., "Impulse reaction resulting from the in-air irradiation of aluminum by a pulsed CO_2 laser," *Journal of Applied Physics*, Vol. 44, 1973, pp. 4079-4085.

[3] Pirri, A. N., Schler, R., and Northam, D., "Momentum transfer and plasma formation above a surface with a high-power CO_2 laser," Applied Physics Letters, Vol. 21, 1972, pp. 79-81.

[4] Simons, G. A., "Momentum Transfer to a Surface When Irradiated by a High-Power Laser," *AIAA Journal*, Vol. 22, 1984, pp. 1275-1280.

[5] Simons, G. A., and Pirri, A. N. "The Fluid Mechanics of Pulsed Laser Propulsion," *AIAA Journal*, Vol.15, 1977, pp. 835-842.

[6] Pirri, A. N., and Monsler, M. J., "Propulsion by Absorption of Laser Radiation," *AIAA Journal*, Vol. 12, 1974, pp. 1254-1261.

[7] Ageev, V. P., Barchukov, A. I., Bunkin, F. V., Konov, V. I., Korobeinikov, V. P., Putjatin, B. V., and Hudjakov, V. M., "Experimental and theoretical modeling of laser propulsion," *Acta Astronautica*, Vol. 7, 1980, pp. 79-90.

[8] Bohn, W. L. "Laser Lightcraft Performance," *Proceedings of SPIE*, Vol. 3885, 2000, pp. 48-53.

[9] Myrabo, L. M., Messitt, D. G., and Mead, Jr., F. B., "Ground and Flight Tests of Laser Propelled Vehicle," *AIAA Paper* 98-1001, 1998.

[10] Sasoh, A., "Laser-Propelled Ram Accelerator," *Journal of Physics IV France*, Vol.10, 2000, pp.41-47.

[11] Katsurayama, H., Ushio, M., Komurasaki, K., and Arakawa, A., "Analytical Study on Flight Performance of an Air-Breathing RP Laser Launcher," AIAA Paper 2004-3585, 2004.

[12] Ushio, M., "A Laser Power Necessary for Air-breathing RP Laser Propulsion," Doctor Thesis, The University of Tokyo (2004).(In Japanese)

[13] Katsurayama, H., "Energy Conversion Process in a Pulse-Laser Boosted Vehicle and its Flight Performance," Doctor Thesis, The University of Tokyo (2004).(In Japanese)

[14] Zel'dovich, Y. B., and Raizer, Yu. P., "Physics of Shock waves and High-temperature Hydrodynamics Phenomena," Dover, NewYork, 2002, p340

[15] Fischer, V. I., Soviet Physics: Technical Physics, Vol.28, 1984.

[16] Nielsen, P. E., "Hydrodynamic calculations of surface response in the presence of laser-supported detonation weaves," *Journal of Applied Physics*, Vol. 46, 1975, pp. 4501-4505.

[17] Jumper, E. J., *Physics of Fluids*, Vol.21, 1978, p. 549.

[18] Kazuyasu, M., "Compressible Flow Dynamics," Rikougakusha, p184, 1994.(In Japanese)

[19] Shiraishi, H., "Numerical Analysis of Generation and Propagation Mechanism of Laser-Supported Detonation in Argon Gas," Doctor thesis, the university of Nagoya,2000.

[20] Raizer,Y.P., "Laser-Inducede Discharge Phenomena," pp.199-204, 1972.

[21] Mori, K., Komurasaki, K. and Arakawa, Y., "Influence of the Focusing f Number on the Heating Regime Transition in Laser Absorption Waves," *J. of Appl. Phys.* 15, (2002), pp.5663-5667.

[22] Mori, K., Komurasaki, K. and Arakawa, Y., "Energy Transfer from a Laser Pulse to a Blast Wave in Reduced-Pressure Air Atmospheres," *J. of Appl. Phys.* 95, (2004), pp.5979-5983.

[23] Bohn, W. L., and Schall, W. O., "Laser Propulsion Activities in Germany" in *Proceedings of First International Symposium on Beamed Energy Propulsion* (*AIP Proceedings*, Vol. 664) ed. by A.V. Pakhomov, 2003, pp. 79-91.

[24] Sasoh, A., Kister, M., Urabe, N., and Takayama, K., "Laser-Powered Launch in Tube," *Transaction of Japan Society of Aeronautical and Space Sciences*, Vol. 46, 2003, pp. 52-54.

[25] Fukuda, A., "Characterization of Post Laser Supported Detonation by Interferometry," Master Thesis, The University of Tokyo (2004).

[26] 村岡克紀, 前田三男"プラズマと気体のレーザー応用計測" 産業図書 (1995).

[27] Richard H. Huddlestone and Stanley L. Leonard "Plasma Diagnostic Techniques" Academic Press, New York(1965).

[28] Sedov, L. I. "*Similarity and Dimension Methods in Mechanics*," Academic Press, New York, 1959.

[29] Bach, G. G., Lee, J. H. "Higher-order perturbation solutions for blast waves," AIAA Journal. 7, (1969), pp.742-744.

[30] Radulescu, M. I., Higgin, A. J., Murray, S. B., Lee, J. H. S., "An Experimental Investigation of the Direct Initiation of Cylindrical Detonations," Journal of Fluid Mechanics, Vol. 480, (2003), pp. 1-24.

[31] Gretler, W., "Blast Waves in Inhomogeneous Atmospheres Including Real Gas and Heat Transfer Effects," Fluid Dynamics Research, Vol. 14 (1994) pp.191-216

[32] Kompaneets, A. S., "A Point Explosion in an Inhomogeneous Atmosphere," Soviet Physics Doklady, 5(1960), pp.46-48